

1  
2 **Elucidating the boundary layer turbulence dissipation**  
3 **rate using high-resolution measurements from a radar**  
4 **wind profiler network over the Tibetan Plateau**  
5  
6

7 Deli Meng<sup>1,2</sup>, Jianping Guo<sup>1,3\*</sup>, Xiaoran Guo<sup>1,\*</sup>, Yinjun Wang<sup>1</sup>, Ning Li<sup>1</sup>, Yuping Sun<sup>1</sup>,  
8 Zhen Zhang<sup>1</sup>, Na Tang<sup>1</sup>, Haoran Li<sup>1</sup>, Fan Zhang<sup>1</sup>, Bing Tong<sup>3</sup>, Hui Xu<sup>1</sup>, Tianmeng Chen<sup>1</sup>

9  
10  
11 <sup>1</sup>*State Key Laboratory of Severe Weather, Chinese Academy of Meteorological Sciences,*  
12 *Beijing 100081, China*

13 <sup>2</sup>*High Impact Weather Key Laboratory of CMA, Changsha 410073, China*

14 <sup>3</sup>*Fujian Key Laboratory of Severe Weather, Fujian Institute of Meteorological Sciences,*  
15 *Fuzhou 350028, China*

16 <sup>4</sup>*State Key Laboratory of Urban and Regional Ecology, Research Center for Eco-*  
17 *Environmental Sciences, Chinese Academy of Sciences, Beijing 100085, China*

18  
19  
20  
21  
22  
23  
24  
25 Correspondence to: Dr/ Prof. Jianping Guo (Email: jpguocams@gmail.com)

26 Dr. Xiaoran Guo (Email: guoxiaoran2018@hotmail.com)

Deleted: <sup>2</sup>

Deleted: Fujian Key Laboratory of Severe Weather, Fujian Institute of Meteorological Sciences, Fuzhou 350028, China

Formatted: Font: (Default) Times New Roman, (Asian) Times New Roman, 12 pt, Italic, Font colour: Text 1, English (US)

Formatted: Superscript

Formatted: Left

Deleted: <sup>4</sup>  
<sub>3</sub>

Deleted:

## Abstract

The planetary boundary layer (PBL) over the Tibetan Plateau (TP) exerts a significant influence on regional and global climate, while its vertical structures of turbulence and evolution features remain poorly understood, largely due to the scarcity of observation. This study examines the vertical profile and daytime variation of turbulence dissipation rate ( $\varepsilon$ ) in the PBL and free troposphere over the TP using the high-resolution (6 min and 120 m) measurements from the radar wind profiler (RWP) network, combined with the hourly data from the ERA5 reanalysis during the period from September 1, 2022 to October 31, 2023. Observational analyses show that the magnitude of  $\varepsilon$  below 3 km under all-sky conditions exhibits a large spatial discrepancy over the six RWP stations over the TP. Particularly, the values of  $\varepsilon$  at Minfeng and Jiuquan over the northern TP and Dingri over the southern TP are roughly an order of magnitude greater than those at Lijiang, Ganzi and Hongyuan over the eastern TP. This could be partially attributed to the difference in land cover across the six RWP stations. In terms of the diurnal variation,  $\varepsilon$  rapidly intensifies from 0900 local standard time (LST) to 1400 LST, and then gradually levels off in the late afternoon. Under clear-sky conditions, both  $\varepsilon$  and planetary boundary layer height ( $z_i$ ) are greater, compared with cloudy-sky conditions, which could be due to the cooling effect by cloud that reduces the solar irradiation reaching the surface. In the lower PBL ( $0.3 \leq z/z_i \leq 0.5$ ), where  $z$  is the height above ground level, the dominant influential factor for the development of turbulence is the surface-air temperature difference ( $T_s - T_a$ ). By comparison, in the upper PBL ( $0.6 \leq z/z_i \leq 1.0$ ), both the  $T_s - T_a$  and vertical wind shear (VWS) affect the development of turbulence. Above the PBL ( $1.0 < z/z_i \leq 2.0$ ), the shear production resulting from VWS dominates the variation of turbulence. Under cloudy-sky conditions, the reduced  $T_s - T_a$  and weakened surface sensible heat flux tend to inhibit the turbulent motion in the PBL. On the other hand, the strong VWS induced by clouds enhances the turbulence above the PBL. The findings obtained here underscore the importance of RWP network in revealing the fine-scale structures of the PBL over the TP and gaining new insight into the PBL evolution.

Deleted: ¶

Formatted: Font: (Default) Times New Roman, (Asian) Times New Roman

Deleted: site

Deleted: of

Deleted: site

Deleted: .

Deleted: This reveals that clouds would suppress the turbulence development and deduce

Deleted: .

Deleted: 2

Deleted: <

Deleted: <

Deleted: )

Formatted: Font colour: Auto

Deleted: <

Deleted: <

Deleted: clouds are found to decrease the surface total solar radiation, thereby re

Deleted: ing

Deleted: This weakened sensible heat flux

Deleted: s

Deleted: within PBL especially

Deleted: lower

Deleted: and decrease the growth rate of PBL

Deleted:  $z_i$

86 **1. Introduction**

Formatted: Font: Times New Roman

87 Turbulence ranks among the most intricate phenomena within the atmosphere, ensuring  
88 that the planetary boundary layer (PBL) remains thoroughly mixed during daylight hours  
89 (Li et al., 2023). As a result, the structure of the PBL is, to a considerable extent, governed  
90 by the evolution of turbulence (Teixeira et al., 2021). Turbulence dissipation rate ( $\epsilon$ )  
91 reflects the amount of turbulent kinetic energy (TKE) that is converted into heat at the  
92 Kolmogorov scale and is a measure of the turbulence intensity (McCaffrey et al., 2017;  
93 Muñoz-Esparza et al., 2018). Proper parameterizations of the turbulence dissipation term  
94 with the aid of observations have great impacts on the forecast skill of weather and climate  
95 models, as  $\epsilon$  strongly affects vertical turbulent mixing through its influence on TKE (Yang  
96 et al., 2017). Accurate estimation of  $\epsilon$  is crucial for understanding the structure of  
97 turbulence in the PBL. To date, a variety of instruments have been used to observe or  
98 retrieve the vertical profiles of  $\epsilon$ , including sodar, radar wind profiler (RWP), radiosonde,  
99 Doppler wind lidar (DWL) and ultrasonic anemometer (Jacoby-Koaly et al., 2002; Dodson  
100 and Griswold, 2021; Lv et al., 2021; Kotthaus et al., 2023). Compared with the DWL, the  
101 RWP exhibits better capability in capturing the turbulence structures in the cloudy sky.  
102 Furthermore, it is hard for radiosondes and ultrasonic anemometers to get the temporal  
103 continuous measurements of atmospheric turbulence, due to the high costs.

Deleted: model  
Deleted: for  
Deleted: the

Deleted: Jacoby-Koaly et al., 2002; Kotthaus et al., 2023;

Deleted: the

Deleted: the

104 The Tibetan Plateau (TP), with an averaged elevation greater than 4,000m above sea  
105 level (ASL) and an area of approximately 2.5 million km<sup>2</sup>, is towering into the lower and  
106 middle troposphere (Huang et al., 2023). By receiving a greater amount of solar shortwave  
107 radiation, the surface layer of the TP can transfer more heat through the PBL to the free  
108 atmosphere (Wang et al., 2015; Ma et al., 2023). The PBL over the TP exhibits strong  
109 convective thermals of warm air and upward motions due to the lower air density and  
110 buoyancy effect, which results in significant turbulence motions and turbulence-convection  
111 interactions with "popcorn" cloud structures (Xu et al., 2002; Xu et al., 2023).  
112 Understanding the statistical behavior of  $\epsilon$  is key to revealing the vertical structure and  
113 evolution of PBL turbulence, which could improve the parameterization of PBL processes  
114 over the TP (Wang et al., 2015; Xu et al., 2019; Zhao et al., 2019; Ma et al., 2023). However,

Deleted: above

Deleted: lar

Deleted: 4000

Deleted: k

Deleted: could

Deleted: Ma et al., 2023;

Deleted: bubbling

Deleted: Ma et al., 2023;

129 due to the limited observations of turbulence profiles, the daytime variation characteristics  
130 of  $\varepsilon$  over the TP and its main influencing mechanisms remain poorly understood.

131 A vast range of previous studies have attempted to figure out the mechanisms behind the  
132 turbulence, but most of them are based on radiosonde measurements or model simulation  
133 or reanalysis data (e.g., Banerjee et al., 2018; Che and Zhao, 2021; Wang et al., 2023a). A  
134 myriad of driving mechanisms is proposed to account for the PBL development over the  
135 TP, such as surface thermal and dynamic forcing, atmosphere stability, among others (Chen  
136 et al., 2016; Lai et al., 2021; Wang and Zhang, 2022; Chechin et al., 2023; Wang et al.,  
137 2023a). It has been demonstrated that the buoyancy term contribution on the southern slope  
138 of the TP is significantly larger than that on the southeastern edge of the TP (Wang et al.,  
139 2015). A larger surface-air temperature difference ( $T_s - T_a$ ) and sensible heat flux  
140 promotes the rapid growth of deep PBL in the western and southern TP (Chen et al., 2013,  
141 2016; Wang et al., 2016; Li et al., 2017a; Zhang et al., 2022).

142 Except for the above-mentioned thermal and dynamic effects, cloud radiative effect is  
143 found to be another significant factor that can dramatically modulate the evolution of  
144 daytime PBL turbulence (Bodenschatz et., 2010; Davis et al., 2020). For instance, cloud  
145 radiative forcing accounts for the rapid morning transition from stable to unstable PBL,  
146 thereby notably affecting the diurnal variation of the PBL (Su et al., 2023). Notably,  
147 longwave radiative cooling at the top of stratocumulus clouds can enhance turbulent  
148 diffusion within the stratocumulus topped PBL (Sun et al., 2016). A recent observational  
149 study suggests that cloud radiative cooling contributed about 32% to turbulent mixing even  
150 near the surface (Huang et al., 2020). In other words, cloud radiative processes, including  
151 entrainment and radiative cooling, can affect the TKE in the atmosphere (Nicholls et al.,  
152 1986; Sedlar et al., 2022; Chechin et al., 2023).

153 The TP is characterized by a high frequency of cumulus clouds which is about five times  
154 the regional mean over the other areas of China (Wang et al., 2015), and the occurrence  
155 frequency of clouds over the TP shows large diurnal and spatial variability, with the  
156 maxima in the afternoon in the eastern TP (Wan et al., 2022). The clouds have been found  
157 to significantly suppress the development of summer PBL in the early afternoon across  
158 China using fine-resolution radiosonde observations (Guo et al., 2019). Under continuous

Deleted: tial

Deleted: remains

Deleted: observed

Deleted: Chechin et al., 2023;

Deleted: Wang et al., 2023a;

Deleted: could

Deleted: Li et al., 2017a;

Deleted: Chen et al (2016) found that the weak atmosphere stability at the top of the mixed layer is a key factor contributing to the rapid growth of the deep turbulence in winter over the TP.

Formatted: Font: Not Italic, Font colour: Text 1

Formatted: Font: Not Italic, Font colour: Text 1

Formatted: Font: Not Italic, Font colour: Text 1

Formatted: Font: Not Italic, Font colour: Text 1

Deleted: Also, Cloud top radiative cooling is one of the most important processes for stratocumulus and PBL turbulence and can serve as a main source of turbulent kinetic energy TKE (Chechin et al., 2023; Nicholls et al., 1986). The growth of the daytime PBL is also modulated by cloud radiative effects besides the surface heating and vertical wind shear (VWS), (Davis et al., 2020).

Deleted: L

Deleted: -

Deleted: boundary layer

Formatted: Font: Not Italic

Deleted: Huang et al (2020) revealed that cloud radiative cooling contributed about 32% to turbulent mixing even near the surface in Hong Kong, although the contribution was relatively weaker compared to surface heating and vertical wind shear VWS

Formatted: Font: Not Italic

Deleted: Su et al (2023) recently suggested that cloud-surface coupling alters the morning transition from stable to unstable boundary layer PBL and thus notably affects the diurnal variation of the boundary layer PBL.

Deleted: cloud radiative effects are found to be another significant factor to modulate the evolution of daytime PBL turbulence (Bodenschatz et., 2010).

Formatted: Font: (Asian) +Body Asian (DengXian)

Deleted: Guo et al. (2019) has revealed that

Deleted: t

Deleted: tends to

Deleted: the



196 cloudy-sky conditions, the convective PBL develops slowly due to the smaller surface  
 197 sensible heat compared to clear-sky conditions (Wang and Zhang, 2022). The turbulence  
 198 motion in the PBL and its dynamic structure contribute to the formation and development  
 199 of the popcorn-like convective clouds (Xu et al., 2002; Wang et al., 2020). Compared with  
 200 eastern China, the more occurrence of low cloud in the afternoon over the TP is found to  
 201 facilitate the PBL development, mainly owing to the lower atmospheric density (Wang et  
 202 al., 2020).

203 However, the differences of turbulence vertical structures between clear-sky and cloudy-  
 204 sky conditions are rarely explored, and the possible mechanism influencing the cloud  
 205 topped PBL turbulence evolution remains unclear. To the best of our knowledge, most of  
 206 the above-mentioned studies over the TP lack high-temporal resolution turbulence profile  
 207 observations. Coincidentally, the RWP network in China provides us a valuable opportunity  
 208 to characterize the PBL turbulence structure over the TP (Guo et al., 2021a). Therefore, the  
 209 main objective of this study is to resolve the above issues over the TP, by using  
 210 observations from the RWP network together with other ground-based meteorological  
 211 measurements and the ERA5 data. We also analyze the joint effect of thermodynamic and  
 212 dynamic on  $\varepsilon$  structure in the daytime (0900–1700 local standard time, LST) PBL through  
 213  $T_s - T_a$  and VWS.

214 The remainder of this manuscript proceeds as follows, Section 2 describes the data and  
 215 methods used in this study. In Section 3, we analyze the spatio-temporal characteristics and  
 216 daytime pattern of  $\varepsilon$  over the TP and investigate the possible thermodynamic and dynamic  
 217 effect on PBL turbulence under clear-sky and cloudy-sky conditions. The summary and  
 218 conclusions are given in section 4.

219

## 220 2. Data and methods

### 221 2.1 The RWP network over the TP

222 In this study, we use the vertical measurements of RWP data with a vertical resolution  
 223 of 120 m and a temporal resolution of 6 min from the RWP network over the TP, which

Deleted: the

Deleted: in the PBL is

Deleted: contributed

Deleted: ors

Deleted: Wang et al., 2020;

Deleted: Based on surface observation, radiosonde, satellite and reanalysis data, Wang et al. (2020) pointed out that higher PBL height and lower lifting condensation level due to lower temperature and lower atmospheric density may enhance low cloud

Deleted: , and

Deleted: in turn influencing influences

Deleted:

Deleted: over the TP

Deleted: turbulence structure

Deleted: elusive

Deleted: there exists a

Deleted: of

Deleted: , which

Deleted:

Deleted: n

Deleted: in

Deleted: vertical wind shear (

Deleted: )

Deleted: -

249 contains six operational ~~stations~~ (Minfeng, Jiuquan, Hongyuan, Ganzi, Lijiang and Dingri)  
250 operated by the China Meteorological Administration (CMA) during the period from  
251 September 1, 2022 to ~~October~~ 31, 2023. The spatial distribution of ~~the~~ RWP network over  
252 the TP is shown in Fig. 1, and ~~detailed information for each RWP station~~, including  
253 longitude, latitude, elevation, and land cover type is given in Table 1. Among these six  
254 RWP ~~stations~~, the Dingri ~~station~~ is located in the foothills of the Himalayas with an  
255 elevation more than 4,300m ~~ASL~~, dominated by the land cover of bare and alpine grassland.  
256 The Lijiang ~~station~~ is located in the southeastern TP characterized by complex terrain with  
257 an elevation of about 2,400m ~~ASL~~. The Ganzi and Hongyuan ~~stations~~ are situated in the  
258 eastern TP, with elevations ranging from 3,300 to 3,500m ~~ASL~~, and whose underlay is  
259 mainly alpine grassland. The Minfen and ~~Jiuquan stations~~ are situated in arid and semi-arid  
260 zones to the north of the TP, with elevations ranging from 1,400 to 1,500m, and their  
261 dominant underlying land cover is mainly bare land. Therefore, these two ~~stations~~ are well  
262 representative of the northern TP.

263 The RWP has the capability to obtain the high-temporal resolution atmospheric  
264 turbulence and wind profiles over the TP compared to the radiosonde and reanalysis, which  
265 makes it possible to analyze the fine PBL structures. The low and medium detection modes  
266 of RWPs can acquire the wind field and turbulence information bellow 5.0 km ~~above~~  
267 ~~ground level (AGL)~~ (McCaffrey et al., 2017; Ruan et al., 2014). The RWP provides the  
268 radial observations (marked as RAD subset), including profiles of radial velocity, doppler  
269 spectral width, and ~~signal-to-noise ratio (SNR)~~. Also provided by the RWP is the real-time  
270 sampling data (marked as ROBS subset), including the profiles of horizontal wind  
271 (direction and speed), vertical velocity, and refractive index structure constant (Liu et al.,  
272 2020). There exist large uncertainties in the profiling measurements from RWP, thus the  
273 quality control for both RAD and ROBS subsets are indispensable before retrieving related  
274 dynamic variables over the TP (Liu et al., 2020; Wang et al., 2023). For instance, the  
275 profiling measurements highly deviate from the truth below 0.5 km AGL and above 5.0  
276 km AGL, which are attributed to the near-surface clutter and significant beam attenuation,  
277 respectively (Guo et al., 2023). Thus, here only the RWP measurements at heights from  
278 0.5 ~~to~~ 5.0 km are utilized for analysis.

Deleted: site

Deleted: November

Deleted: the

Deleted: site

Deleted: site

Deleted: site

Deleted: above sea level (AGLASL)

Deleted: site

Deleted: AGL

Deleted: site

Deleted: AGL

Deleted: Dunhuang

Deleted: site

Deleted: site

Deleted: signal to noise

Deleted: ratio

Deleted: km

297 **2.2 *Miscellaneous meteorological data***

298 In this study, the hourly ground-based meteorological variables, including 2m air  
299 temperature ( $T_a$ ), ground surface temperature ( $T_s$ ), pressure and cloud cover, are derived  
300 from the six automatic weather stations over the TP. Also, 1 min rainfall observations from  
301 rain gauges are used to minimize the potential influence of rainfall on the profiling  
302 measurements from RWP. All these meteorological datasets are subjected to strict data-  
303 quality control by the National Meteorological Information Center (NMIC) of the CMA  
304 (Wang et al., 2023b). In addition, the hourly temperature data at pressure levels from the  
305 ERA5 reanalysis data is also used in this study (Hersbach et al., 2020).

306

307 **2.3 *Methods***

308 **2.3.1 *Retrieval of turbulence dissipation rate***

309 As a widely used ground-based equipment for detecting atmospheric wind profile (Liu  
310 et al., 2020), RWP has the advantage to estimate  $\epsilon$  since it could measure Doppler velocity  
311 spectrum in the radar volume where the turbulence parcel motion accounts for the spectral  
312 width broadening (Jacoby-Koaly et al., 2002; White, 1999). In this study, the spectral width  
313 method is applied to retrieve  $\epsilon$  from the RAD subset based on the underlying assumption  
314 that turbulence is isotropic, and the contributions to the spectral width from turbulent and  
315 non-turbulent process are independent of each other (Solanki et al., 2022; White, 1999).

316 The major steps for  $\epsilon$  retrieval can be summarized as follows: (1) the spectral width  
317 variance consisting of the turbulence and non-turbulence variance is obtained from the  
318 spectral width measurements. (2) The non-turbulence broadening variances are  
319 decomposed into beam broadening variance due to the finite width of the beam, shear  
320 broadening variance generated by the presence of a wind gradient, and broadening variance  
321 arising from data processing, among others (Nastrom, 1997). (3) The turbulent broadening  
322 variance ( $\sigma_t^2$ ) is extracted from the spectral width variance by excluding the above-  
323 mentioned non-turbulence broadening variances. (4)  $\epsilon$  is estimated from  $\sigma_{t,r}^2$  (White et al.,  
324 1999). For more details about the spectral width method, refer to the references (Jacoby-  
325 Koaly et al., 2002; McCaffrey et al., 2017; Nastrom, 1997; Solanki et al., 2021).

Deleted: Other

Deleted: m

Deleted: site

Deleted: -

Deleted: China Meteorological Administration

Deleted: hypothesis

Deleted: 2021

Deleted: above mentioned

Deleted: the

Deleted: turbulent broadening variance with the main assumption of isotropic and homogeneous turbulence, as well as Gaussian antenna symmetric illumination function and Gaussian radial response of the receiver

Deleted: for

340 ~~One caveat of the above-mentioned methods used to estimate  $\epsilon$  lies in its sensitivity to~~  
 341 ~~the uncertainty in measuring horizontal wind speed, and the occurrence of negative value~~  
 342 ~~of  $\sigma_t^2$ , resulting in negative  $\epsilon$  (i.e., invalid retrieval and should be discarded), which is~~  
 343 ~~previously documented (e.g., Chen et al., 2021; McCaffrey et al., 2017). It's noteworthy~~  
 344 ~~that  $\epsilon$  estimates derived from the RWP lacks validation against in situ  $\epsilon$  measurements~~  
 345 ~~from sonic anemometer in the aircraft or tower. This is another factor causing uncertainties~~  
 346 ~~that needs to be addressed in the future.~~

### 347 2.3.2 Estimation of planetary boundary layer height

348 The PBL height (hereafter referred to as  $z_i$ ) is an important parameter for characterizing  
 349 fine vertical structure of the PBL, which has important implications for the air mass  
 350 exchange between the Earth's surface and the atmosphere aloft, thus affecting cloud  
 351 development and air pollutant dispersion (Dai et al., 2014; Dodson and Griswold, 2021;  
 352 Guo et al., 2021a; Li et al., 2017b; Wang et al., 2022).

353 Here daytime  $z_i$  at each RWP station is retrieved from the original SNR profiles from  
 354 the RAD subset based on the improved threshold method (ITM), which is originally  
 355 proposed by Liu et al. (2019). The steps are briefly outlined as follows. First of all, the  
 356 original SNR profiles are normalized, leading to the profile of normalized SNR (NSNR),  
 357 which is expected to avoid instrumental inconsistencies. Secondly, the NSNR threshold is  
 358 set to 0.75 based on the  $z_i$  estimated by the radiosonde measurements at the same station.  
 359 Thirdly, the profile of NSNR is scanned downward from the top to the ground surface.  
 360 Finally,  $z_i$  is determined as the height where the NSNR profile is greater than 0.75 for the  
 361 first time. For more details for the ITM, refer to Liu et al. (2019).

362 It is not optimal to retrieve  $z_i$  directly from the RWP measurements during nighttime,  
 363 when the turbulence is weaker and SNR is stronger, leading to an overestimation of  $z_i$   
 364 (Duncan et al., 2022). The accuracy of the SNR data from RWP directly affects the  
 365 accuracy of  $z_i$ . The  $z_i$  estimation for the ITM is particularly applicable in the daytime  
 366 PBL (Bianco et al., 2008; Collaud Coen et al., 2014). The presence of clouds is proved to  
 367 bring about uncertainty in  $z_i$  retrievals from the ITM, due to the challenge in identifying  
 368 the peak from the NSNR profile (Angel et al., 2024). Notably, a convective cloud is  
 369 accompanied by strong turbulence, which results in its boundary being misjudged as  $z_i$ .

- Deleted: The
- Deleted: It's note that
- Formatted ... [2]
- Deleted: ion of
- Deleted: is highly ...ensitivitye...to the uncertainty in ... [4]
- Formatted ... [11]
- Formatted ... [3]
- Deleted: turbulence dissipation rate ( $\epsilon$ )
- Deleted: the uncertainty of the calculation of
- Formatted ... [5]
- Formatted ... [6]
- Deleted: )
- Deleted: When the spectral width method is used to cal ... [8]
- Moved up [2]: (Chen et al., 2021; McCaffrey et al., 2017
- Moved (insertion) [2]
- Deleted: (Chen et al., 2021; McCaffrey et al., 2017
- Formatted ... [7]
- Deleted: There is still a lack of evaluation of
- Formatted ... [9]
- Deleted: with...those obtained from ... [10]
- Formatted ... [11]
- Deleted: aircraft, ...onic anemometer in the aircraft or ... [12]
- Formatted ... [13]
- Deleted: planetary boundary layer
- Deleted: the
- Deleted: site...tation is derived ... [14]
- Deleted: signal-to-noise ratio (...NR) ... [15]
- Deleted: derived by...roposed by Liu et al. (2019). Th ... [16]
- Deleted: site...tation. Thirdly, the profile of NSNR is ... [17]
- Deleted: ultimately ...s determined as the height where ... [18]
- Deleted: The RWP performs well during cloud-free ... [19]
- Formatted ... [20]
- Deleted: derive
- Formatted ... [21]
- Formatted ... [22]
- Deleted: when the  $z_i$  might be lower than the first ave ... [23]
- Formatted ... [24]
- Deleted: ....r
- Formatted ... [25]
- Formatted ... [26]
- Deleted: conditions
- Formatted ... [27]
- Deleted: increase...s proved to bring abouts ... [28]
- Deleted: CBLH
- Deleted: for...the ITM, due to the challenge in identif ... [29]
- Deleted: SNR ...eak from the NSNR profile ... [30]
- Formatted ... [31]

483 2.3.3 Vertical wind shear

484 The ROBS subset is used to calculate VWS, which is an important parameter that  
485 presents the dynamical effect on the development of PBL (Zhang et al., 2020). VWS is  
486 given by.

$$VWS = \left[ \left( \frac{\partial u}{\partial z} \right)^2 + \left( \frac{\partial v}{\partial z} \right)^2 \right]^{1/2} \quad (1)$$

487 where  $u$  and  $v$  denote zonal and meridional wind component, respectively,  $z$  denotes the  
488 sample height AGL.

489 2.3.4 Classification of cloudy- and clear-sky conditions

490 Using RWP combined with the ground-based cloud cover observations at each station,  
491 the effect of clouds on daytime variations of PBL turbulence and  $z_i$  over the TP are  
492 investigated. Firstly, the 1 min precipitation and 6 min RWP data are time-matched to  
493 remove the profile data half an hour before and after the precipitation to obtain non-  
494 precipitation data (Wu et al, 2023). Then, all-sky conditions are defined as non-  
495 precipitation hours. Finally, the clear-sky (cloudy-sky) conditions are identified as hours  
496 with the cloud fraction less (greater) than 30% (80%), respectively (Guo et al., 2016;  
497 Solanki et al., 2021).

498 2.3.5 Calculation of the gradient Richardson number

499 The evolution of turbulence in the PBL has been previously recognized to be closely  
500 associated with atmospheric stability (Chechin et al., 2023; Chen et al, 2013; Lai et al.,  
501 2021; Muhsin et al., 2016). Therefore, we take the gradient Richardson number ( $Ri$ ) as a  
502 variable to characterize atmospheric stability and the formation of turbulence over the TP.  
503 Following Stull (1988),  $Ri$  is formulated as follows:

$$Ri = \frac{g}{\theta_v} \frac{\partial \theta_v / \partial z}{(\partial u / \partial z)^2 + (\partial v / \partial z)^2} \quad (2)$$

504 where  $\theta_v$  is the virtual potential temperature from ERA5,  $u$  and  $v$  are the hourly zonal  
505 and meridional wind components derived from RWP, respectively,  $g$  is the gravitational  
506 acceleration, and  $z$  represents the sample height AGL.

507

Deleted: vertical wind shear (VWS)  
Deleted: can be calculated  
Deleted: as follows  
Deleted: .  
Formatted: Font: (Asian) +Body Asian (DengXian)

Deleted: site

Deleted: -

Deleted: -

### 515 3. Results and discussion

#### 516 3.1 Spatio-temporal distributions of daytime PBL turbulence dissipation rate

517 Both the PBL turbulence dissipation rate and  $z_i$  have significant diurnal variations over  
518 mountain and urban areas (Adler et al., 2014; Liu et al., 2019; Solanki et al., 2021; Yang  
519 et al., 2023). Since the longitude of the six stations over the TP ranges from 82.7°E to  
520 102.6°E, it is necessary to use the LST to accurately capture the daytime variations of the  
521 PBL and make a comparison between different stations.

522 Figure 2 presents a comprehensive overview of the  $\varepsilon$  profile at 6 min intervals and  
523 hourly averaged  $z_i$  in lower troposphere at heights from 0.5 to 3.0 km for six RWP stations  
524 over the TP during the period from September 1, 2022 to October 31, 2023. As shown in  
525 the right panels of Fig. 2,  $\varepsilon$  generally decrease with increased height at all six RWP  
526 stations. The magnitude of  $\varepsilon$  and its vertical structures during the daytime at both Minfeng  
527 and Jiuquan stations over the northern TP and at Dingri station over the southern TP stand  
528 in stark contrast to those RWP stations (i.e., Lijiang, Ganzi and Hongyuan) in the eastern  
529 TP. It is apparent that  $\varepsilon$  exhibits a large spatial discrepancy. In terms of the latitudinal  
530 variation, the one-year averaged  $\varepsilon$  at the RWP stations in the east part of TP is smaller  
531 than in the western part of TP. In terms of the meridional variation,  $\varepsilon$  at the two RWP  
532 stations in the northern TP have a significantly larger magnitude than the other four stations.  
533 In particular, the maximum mean value of daytime  $\varepsilon$  is found at Minfeng and Jiuquan  
534 in the northern TP, which reaches values up to  $10^{-3.59} \text{ m}^2 \text{ s}^{-3}$  and  $10^{-3.73} \text{ m}^2 \text{ s}^{-3}$ , respectively.  
535 By comparison, the lowest value of  $\varepsilon$  is found in the eastern TP, with the mean values of  
536  $10^{-4.06} \text{ m}^2 \text{ s}^{-3}$ ,  $10^{-4.30} \text{ m}^2 \text{ s}^{-3}$  and  $10^{-4.22} \text{ m}^2 \text{ s}^{-3}$  at Lijiang, Hongyuan and Ganzi, respectively.  
537 Meanwhile, the mean magnitude of  $\varepsilon$  at Dingri in the southern TP lies between the  
538 magnitude of  $\varepsilon$  in the northern and eastern TP, which is  $10^{-3.88} \text{ m}^2 \text{ s}^{-3}$ .

539 Overall, the spatial distribution of the  $z_i$  at all six RWP stations is clearly dependent on  
540 geographical location (Fig. 2), which resembles that of the  $\varepsilon$ . The geographic pattern of  
541  $z_i$  from RWP agrees well with those from radiosonde measurements (Che and Zhao, 2021)  
542 and reanalysis (Slättberg, 2022). Of the six RWP stations, Dingri is located in the northern  
543 foothills of the Himalayas with an altitude of over 4300 m, where the bare land type results

Formatted: Font: Times New Roman

Deleted: site

Deleted: is

Deleted: d

Deleted: Local Standard Time (

Deleted: )

Deleted: site

Deleted: km

Deleted: site

Deleted: November

Moved (insertion) [1]

Deleted: site

Deleted: site

Deleted: site

Deleted: site

Moved up [1]: As shown in the right panels of Fig. 2,  $\varepsilon$  generally decrease with increased height at all six RWP sites.

Deleted: r

Deleted: west-east and north-southern

Deleted: difference

Deleted: under all-sky conditions

Deleted: ongtitudinal

Deleted: latitudinal

Deleted: in

Deleted: that of

Deleted: at

Deleted: RWP sites

Deleted:  $\varepsilon$  exhibits a decreasing trend from west to east at both Minfeng and Jiuquan sites along the altitude belt of 38°N, so does the RWP sites of Dingri, Lijiang, Ganzi and Hongyuan along the altitude belt of 30°N

Deleted: site

Deleted: site

Deleted: in the height range of 0.5 to 3.0 km

Deleted: least magnitude

Deleted:  $z_i, z_i$

Deleted: site

Formatted: Font: (Asian) +Body Asian (DengXian)

Formatted: Font: Not Italic, Font colour: Text 1

579 in a large surface sensible heat flux. This, together with the lowest atmospheric density,  
580 leads to the highest daytime mean value of  $z_i$  up to 2.10 km (Wang et al., 2015). The land  
581 surfaces at the Minfeng and Jiuquan stations in the northern TP are dominated by barren  
582 and relatively homogenous terrain, in sharp contrast to the highly vegetated terrain at the  
583 Ganzi and Hongyuan stations in the eastern TP (Fig. 1). The sparse vegetation in the  
584 northern TP generally comes with large Bowen ratio during the daytime, which tends to  
585 produce larger sensible heat flux compared to that in the eastern TP. The increased  
586 turbulence intensity in the PBL is generally associated with larger sensible heat flux, which  
587 has been reported by previous studies (Wang et al., 2016; Zhang et al., 2022). Therefore,  
588 the spatial and temporal variation of daytime  $\varepsilon$  over the TP are affected by the underlying  
589 surface type and air density.

590 Regarding the daytime pattern of turbulence (all six panels with color shading in Fig. 2),  
591 the turbulence over the TP shows a pronounced signature of single-peak variability. During  
592 the period 0900–1100 LST, the magnitude of  $\varepsilon$  at all six RWP stations is relatively weak.  
593 From 1100 LST onward, with the increase of downward solar shortwave radiation, surface  
594 sensible heat flux gradually rises, which leads to acceleration of turbulence mixing  
595 processes. Then,  $\varepsilon$  reaches peak in the early afternoon (1300–1500 LST). Afterwards,  
596 during the later afternoon (1500–1700 LST),  $\varepsilon$  diminishes gradually. Likewise,  $z_i$  almost  
597 follows the same daytime variation pattern of  $\varepsilon$ .

598 On the seasonal scale, the turbulence at the six RWP stations is characterized by  
599 significant variability, which is shown in Fig. S1. To be more specific,  $\varepsilon$  reaches the  
600 maximum in summer with the highest  $z_i$ , while touches the minimum in winter at Minfeng  
601 and Jiuquan. At the remaining four stations, the strongest  $\varepsilon$  is found in spring, as opposed  
602 to the weakest  $\varepsilon$  in autumn.

603 The above-mentioned findings imply that the turbulence intensity at the RWP stations  
604 over the northern and western TP is about one order of magnitude greater than that in the  
605 eastern TP. To further investigate the possible reasons for this significant difference in  $\varepsilon$ ,  
606 the relationships between  $T_s - T_a$  and  $\varepsilon$  for different regions are presented in Fig. 3. The  
607 mean value of  $T_s - T_a$  in the northern and southern TP is 14.29°C, which is greater than  
608 that of eastern TP with the value of 11.26°C (Fig. 3a). The mean daytime  $\varepsilon$  for the two

Formatted: Font colour: Text 1

Deleted: Of the six RWP sites, Dingri is located in the northern foothills of the Himalayas at an altitude of over 4300 m, where the bare land type of the subsurface results in a large surface sensible heat flux, which together with the lowest atmospheric density leads to the highest daytime mean value of  $z_i$  up to 2.10 km. Compared with Dingri at the same latitude, although Lijiang has a bare ground and a relatively smaller sensible heat flux,  $z_i$  with the value of 1.40 km is lower than that of the Dingri at the same latitude due to the lower altitude and higher air density (Wang et al., 2015).

Formatted: Font colour: Text 1

Formatted: Font: Not Italic, Font colour: Text 1

Deleted: site

Deleted: site

Deleted: site

Formatted: Indent: First line: 2 ch, Space Before: 0 pt, After: 6 pt

Deleted: (Fig. S1)

Deleted: tions

Deleted: are

Deleted: strongest

Deleted: are weakest

Deleted:

Deleted: Hongyuan and Ganzi

Deleted: are strongest

Deleted: and

Deleted: For Dingri and Lijiang,  $\varepsilon$  are strongest in spring and summer, and weakest in autumn.

Deleted: As shown in ure, in lower troposphere maximum are observed at (0.029) (0.027), as compared with the minimum slope of this near-surface thermal properties have nothing to do with  $\varepsilon$  in the eastern TP Besides, the potential impact of VWS on  $\varepsilon$  examined, which is shown Fig. S3. Overall, VWS is found to positively the range, differing by RWP sites. The maximum slope value of 67.45 is found at Hongyuan. Therefore, it can be inferred that atmospheric dynamic effect induced by VWS dominates the variability of  $\varepsilon$  at regions with the same underlying terrain and land over as Hongyuan. TPBL

Deleted: results

Deleted: site

Deleted:



647 regions reaches up to  $10^{-3.74} \text{ m}^2 \text{ s}^{-3}$  and  $10^{-4.20} \text{ m}^2 \text{ s}^{-3}$ , respectively (Fig. 3b). Additionally,  $\varepsilon$   
648 is significantly and positively correlated with  $T_s - T_a$  ( $R > 0.35$ ,  $p < 0.005$ ), which  
649 illustrates that the thermal forcing makes an important contribution to turbulence  
650 development in the TP (Fig. 3c-d). As shown in Fig. S2, there is a positive correlation  
651 between the  $T_s - T_a$  and  $\varepsilon$ , indicating that the thermal effect of the  $T_s - T_a$  can promote  
652 the development of turbulence in at heights from 0.5 to 3.0 km under all-sky conditions.  
653 However, the relationship varies significantly between each RWP station. The slope values  
654 of the regression coefficients for the other five RWP stations, except for Hongyuan are all  
655 greater than 0.015. The maximum slope values are observed at Lijiang (0.029) and Dingri  
656 (0.027) in the southern TP, as compared with the minimum slope of 0.007 at Hongyuan.  
657 This suggests that near-surface thermal properties have nothing to do with  $\varepsilon$  at Hongyuan  
658 in the eastern TP.

659 Besides, the potential impact of VWS on  $\varepsilon$  is also examined, which is shown Fig. S3.  
660 Overall, VWS is found to positively correlate with  $\varepsilon$  at heights from 0.5 to 3.0 km under  
661 all-sky conditions, differing by RWP stations. The maximum slope values are observed at  
662 Lijiang (79.34) and Hongyuan (68.56), as compared with the minimum slope of 1.15 at  
663 Minfeng. Therefore, it can be inferred that atmospheric dynamic effect induced by VWS  
664 dominates the variability of  $\varepsilon$  at regions with the same underlying terrain and land over  
665 as Hongyuan.

### 666 **3.2 Characteristics of daytime PBL turbulence dissipation rate under clear- and** 667 **cloudy-sky conditions.**

668 The influence of clouds on the PBL properties has been discussed and analyzed in  
669 previous studies (e.g., Guo et al., 2016; Huang et al., 2023; Ma et al., 2023; Schumann et  
670 al., 1991; Yu et al., 2004). To reveal the potential impact of clouds on the PBL  $\varepsilon$  over the  
671 TP, the comparison analyses between clear- and cloudy-sky conditions are presented in  
672 this section. Figure 4 shows the daytime cycle of mean  $\varepsilon$  profile and  $z_i$  averaged over the  
673 six RWP stations under all-, clear- and cloudy-sky conditions. Overall, both the profile of  
674  $\varepsilon$  and  $z_i$  under all-sky conditions over the TP present distinct single-peak variations, and  
675 their peaks approximately occur at 1400 LST (Fig. 4a). The daytime averaged  $\varepsilon$  below 3.0

Deleted: s

Deleted: and 3d

Deleted: site

Deleted: site

Deleted: site

Deleted: ¶

Overall, the spatial distribution of the  $z_i$  at all six RWP sites is clearly dependent on geographical location (Fig. 2), which resembles that of the  $\varepsilon$ . The geographic pattern of  $z_i$  from RWP agrees well with those from radiosonde measurements (Che and Zhao, 2021) and reanalysis (Slättberg, 2022). 0.01 k1.40 kThe land surfaces at both Minfeng and Jiuquan sites in the northern TP are dominated by barren and relatively homogenous terrain, in sharp contrast to the highly vegetated underlying terrain at both Ganzi and Hongyuan sites in the eastern TP (Fig. 1). The sparse vegetation in the northern TP generally comes with large Bowen ratio during the daytime, which tends to produce larger sensible heat flux compared to that in the eastern TP. The increased turbulence intensity in PBL is generally associated with larger sensible heat flux, which has been reported by previous studies (Wang et al., 2016; Zhang et al., 2022). ThusTherefore, we argue that the spatial and temporal variation and magnitude of  $\varepsilon$  over the TP are most likely relevant toaffected by the underlying surface type.¶ Regarding the daytime pattern of turbulence (all six panels with color shading in Fig. 2), the turbulence over the TP shows a pronounced signature of single-peak variability. During the period 0900–1100 LST, the magnitude of  $\varepsilon$  at all six RWP sites is relatively weak. From 1100 LST onward, with the increase of downward solar shortwave radiation, surface sensible heat flux gradually rises, which leads to acceleration of turbulence mixing processes. Then,  $\varepsilon$  reaches peak in the early afternoon (1300–1500 LST). Afterwards, during the later afternoon (1500–1700 LST),  $\varepsilon$  diminishes gradually. Likewise,  $z_i$  almost follows the same daytime variation pattern of  $\varepsilon$ .¶

Formatted: Font: Times New Roman

Deleted: evolution

Deleted: site



715 km AGL is  $10^{-3.95} \text{ m}^2 \text{ s}^{-3}$ , and mean  $z_i$  is 1.47 km, respectively. There is a significant  
716 positive correlation between  $\varepsilon$  and  $z_i$  during the daytime ( $R=0.63$ ,  $p<0.01$ ).

717 Under clear-sky condition, the daytime mean  $\varepsilon$  is  $10^{-3.88} \text{ m}^2 \text{ s}^{-3}$  (Fig. 4b). During the  
718 period 1300–1500 LST,  $\varepsilon$  ranges from  $10^{-3.43}$  to  $10^{-2.82} \text{ m}^2 \text{ s}^{-3}$  ( $10^{-4.17}$  to  $10^{-3.40} \text{ m}^2 \text{ s}^{-3}$ ) at  
719 heights from 0.5 km (1.0 km) to 1.0 km (2.0 km) in lower (upper) PBL. Thus, the well-  
720 mixed turbulence maintains the development of PBL in the early afternoon. By comparison,  
721 under cloudy-sky condition (Fig. 4c), the daytime mean value of  $z_i$  can reach up to 1.4 km,  
722 which is 0.12 km lower than that of clear-sky conditions. This means that the clouds would  
723 suppress the development of the PBL turbulence in the early afternoon which has been  
724 observed by the radiosonde observations described in Guo et al. (2016).

725 It is well known that there exists diurnal variation in PBL. To better reveal the  
726 mechanism how a myriad of geophysical parameters affect turbulence, the height-revolved  
727  $\varepsilon$  retrievals are further normalized by the average PBL height. As noted above, the valid  
728 minimum altitude of the RWP is 0.5 km at 120 m vertical resolution, and the maximum  $z_i$   
729 is approximately 2.0 km (Figs. 2&4).  $z$  is normalized by  $z_i$  to provide a nondimensional  
730 vertical coordinate for  $\varepsilon$ . It follows that  $z/z_i$  is great than 0.25, and the range of  $z/z_i$  is  
731 set from 0.3 to 2.0 for the following analyses.

732 The probability density distribution (PDF) of  $\varepsilon$  in the PBL ( $0.3 \leq z/z_i \leq 1.0$ ) and  
733 above the PBL ( $1.0 < z/z_i \leq 2.0$ ) under all-, clear- and cloudy-conditions are given in Fig. 5.  
734 Overall, the mean  $\varepsilon$  are  $10^{-3.82}$ ,  $10^{-3.79}$  and  $10^{-3.85} \text{ m}^2 \text{ s}^{-3}$  at the height range of  $0.3 \leq z/z_i \leq 2.0$   
735 under all-, clear- and cloudy-sky conditions, respectively (Fig. 5a). Within the PBL (Fig.  
736 5b), the mean  $\varepsilon$  under clear-sky conditions ( $10^{-3.27} \text{ m}^2 \text{ s}^{-3}$ ) is greater than that of under  
737 cloudy-sky conditions ( $10^{-3.36} \text{ m}^2 \text{ s}^{-3}$ ), and the standard deviation of  $\varepsilon$  under clear-sky  
738 conditions is slightly greater than that under cloudy-sky conditions. This illustrates that  
739 clouds can significantly inhibit the turbulence intensity in the PBL, with the value of  $\Delta\varepsilon$   
740 between clear- and cloudy-sky conditions is  $-10^{-4.0} \text{ m}^2 \text{ s}^{-3}$ . However, above the PBL (Fig.  
741 5c),  $\varepsilon$  presents normal distribution characteristics, and there is no significant difference  
742 between the mean  $\varepsilon$  under clear- and cloudy-sky conditions.

- Deleted: 1472
- Deleted: is ...anged ... [32]
- Deleted: U
- Deleted: 1415 ...4 km, which is 117 ... [33]
- Deleted: The 50, 75, and 95 quartiles of the daytime  $z_i$  over the six RWP sites under all-sky conditions are 1472m, 1984m, and 3117m, respectively. Therefore, it can be seen that when the 95 quantile of  $z_i$  is selected as the maxi ... [34]
- Formatted: Font: Not Italic
- Deleted: ¶
- Formatted: Font: (Asian) Times New Roman
- Deleted: ¶
- Deleted: F
- Deleted: mean
- Formatted ... [35]
- Formatted ... [36]
- Deleted: ...and Fig. ... [37]
- Moved (insertion) [4]
- Deleted: of  $z/z_i$
- Deleted: ¶ ... [38]
- Formatted: Not Highlight
- Formatted ... [39]
- Deleted: . Therefore,... and the range of the profiles of ... [40]
- Formatted: Not Highlight
- Formatted ... [41]
- Deleted: ranges...is set from 0.3 to 2.0 for the follow ... [42]
- Moved up [4];  $z$  is normalized by  $z_i$  to provide a
- Deleted: ¶ ... [43]
- Deleted: more
- Deleted:
- Deleted: ,
- Deleted: t
- Deleted:  $0.2 \dots 3 \leq \leq$  ... [44]
- Deleted:  $\leq$
- Deleted:  $\leq$
- Deleted:  $< z/z_i < 1.0$
- Deleted: ¶ ... [45]
- Deleted:  $0.2 \dots 3 \leq \leq$  ... [46]
- Deleted:  $\leq$
- Deleted:  $<$
- Deleted:  $<$

853 To examine the overall impact of clouds on the vertical structure of turbulence within  
 854 and above the PBL, Figure 5d shows the normalized contoured frequency by altitude  
 855 diagram (NCFAD) of the  $\Delta\varepsilon$  for normalized ( $z/z_i$ ) profiles of  $\varepsilon$  between cloudy-sky and  
 856 clear-sky conditions. Within the PBL,  $\Delta\varepsilon$  is negative, and  $|\Delta\varepsilon|$  generally decrease with  
 857 increased  $z/z_i$ , where  $\Delta\varepsilon$  is  $-10^{-4.3} \text{ m}^2 \text{ s}^{-3}$  at  $z/z_i=0.5$ , and  $-10^{-5.0} \text{ m}^2 \text{ s}^{-3}$  at  $z/z_i=1.0$ ,  
 858 respectively. This suggests that clouds may weaken turbulence within the PBL (Fig. 4b-c),  
 859 especially in the lower PBL ( $z=820\text{m}$ ,  $z/z_i<0.5$ ). ~~Figure S4 further shows the distinct~~  
 860 ~~spatial variability of cloud effect on  $\varepsilon$  across the six RWP stations. Particularly, the~~  
 861 ~~turbulence is weakened by clouds within the PBL at Minfeng and Jiuquan in the northern~~  
 862 ~~TP, as opposed to the enhanced  $\varepsilon$  within the PBL at Ganzi and Lijiang. This suggests that~~  
 863 ~~the cloud impact on  $\varepsilon$  is much complicated than expected. One of the reasons could be~~  
 864 ~~concerned with the cloud life stage, which is not dealt with in this present study. On top of~~  
 865 ~~the life stage, the cloud impact on  $\varepsilon$ , in combination with  $T_s - T_a$  and VWS, exhibits a~~  
 866 ~~distinct altitude dependence, differing by RWP stations (Fig. S5).~~

867

### 868 **3.3. Potential factors Influencing daytime PBL turbulence dissipation rate**

#### 869 **3.3.1 Surface-air temperature difference**

870 The vertical structure of PBL  $\varepsilon$  and  $z_i$  over the TP show obvious spatial differences in  
 871 the context of a complex subsurface. The diverse land cover types lead to differences in  
 872 surface albedo and soil moisture, which in turn lead to distinctions in thermodynamic  
 873 characteristics such as sensible heat flux (Ma et al., 2023). Buoyant production driven by  
 874 solar heating from the surface is one of the dominant sources generating turbulence in the  
 875 convective PBL. The surface sensible heat flux is an important thermodynamic factor that  
 876 affects the buoyant convective processes (Stull, 1988). Meanwhile, previous studies (e.g.,  
 877 Wang et al., 2022; Yang et al., 2023) have suggested that  $T_s - T_a$  can serve as a good  
 878 proxy for the sensible heat flux. There are not sensible heat flux measurements at six RWP  
 879 stations in this study, and thus we directly take  $T_s - T_a$  as a proxy thermodynamic variable  
 880 to analyze its potential connection to variation of PBL turbulence.

Deleted: s  
 Deleted: and 4  
 Deleted: ¶  
 Deleted: .  
 Deleted: ),  
 Deleted: under cloudy-sky conditions  
 Deleted: is  
 Deleted: and above  
 Deleted: , is enhanced within the PBL at  
 Deleted: .

Deleted: From Fig. S5, it can be seen that the turbulence characteristics of different heights affected by  $T_s - T_a$  and VWS are obviously different. For  $T_s - T_a$ , the slope values of the regression coefficient nearly decrease linearly with height and is close to zero near the top of the PBL. For VWS, the slope values increase with height within the PBL and decrease above the PBL. At Dingri, the thermal and dynamic effect on turbulence is stronger under the clear-sky conditions.¶

Deleted: site

903 Figure 6 shows the magnitude of  $\varepsilon$  varies as a function of  $T_s - T_a$  for all six stations,  
 904 within ( $0.3 \leq z/z_i \leq 1.0$ ) and above ( $1.0 < z/z_i \leq 2.0$ ) the PBL, under all, clear- and cloudy-  
 905 sky conditions, respectively.  $T_s - T_a$  are first classified into five bins, which are then  
 906 statistically analyzed against the corresponding  $\varepsilon$  averaged for  $z/z_i$  values between 0.3  
 907 and 2.0 to obtain regression equations incorporating slopes. Further, Table 2 shows the  
 908 scatter plots between  $\text{Log}_{10}\varepsilon$  (Figure 6) and  $T_s - T_a$  (and VWS, Figure 7) at different  
 909 altitude ranges under all-, clear- and cloudy-sky conditions.  $\text{Log}_{10}\varepsilon$  is found to be linearly  
 910 correlated with  $T_s - T_a$  (and VWS) ( $p < 0.05$ ). The surface sensible heat flux generally  
 911 increases with increased  $T_s - T_a$ , thus the increased  $T_s - T_a$  intensifies the turbulence in  
 912 PBL ( $0.3 \leq z/z_i \leq 1.0$ ), which is shown in Fig. 6b, e, h. Within the PBL,  $\varepsilon$  is also positively  
 913 correlated with  $T_s - T_a$  whose slope values are larger than those at  $0.3 \leq z/z_i \leq 2.0$ . As  
 914  $T_s - T_a$  rises, the larger surface sensible heat flux would lead to enhanced buoyancy  
 915 process and turbulent motion within the PBL. On the other hand,  $\varepsilon$  above the PBL is  
 916 negatively correlated with  $T_s - T_a$  (Figs. 6c, f, i). This suggests that  $T_s - T_a$  dramatically  
 917 affects the development of turbulence within the PBL, whereas it has little effect on the  
 918 turbulence above the PBL.

919 Within the PBL, the magnitude of slope (slope=0.019) under clear-sky conditions is  
 920 larger than that of under-cloudy conditions (slope = 0.015) as shown in Figs. 6e and 6h.  
 921 This implies that  $T_s - T_a$  is the governing parameter rather than cloud cover affecting the  
 922 PBL turbulence, particularly under the clear-sky conditions. Given that turbulence in the  
 923 mixed PBL over the TP is usually driven by convection (Xu et al., 2023), as  $T_s - T_a$   
 924 decreases when clouds are present, less heat is transferred from the surface to the  
 925 atmosphere, reducing the buoyancy flux and leading to weaker turbulence in the PBL,  
 926 especially for the lower PBL ( $0.3 \leq z/z_i \leq 0.5$ ), as shown in Figures 4b and 4c. Consequently,  
 927 the clouds tend to suppress the development of PBL (Fig. 5a) and reduce  $z_i$ .

### 928 3.2.2 Vertical wind shear

929 Besides  $T_s - T_a$ , VWS is another crucial dynamic parameter that is related to the  
 930 mechanical turbulence within the PBL. Similar to Fig. 6, Figure 7 presents the relationship  
 931 between  $\varepsilon$  and VWS (both normalized by  $z_i$ ) within and above the PBL under all-, clear-

- Deleted: site
- Deleted: 0.2
- Deleted:  $\leq$
- Deleted:  $\leq$
- Deleted:  $<$
- Deleted:  $<$
- Deleted:  $\leq$
- Deleted:  $\leq 1$
- Deleted:  $<$
- Deleted: 0.2

- Deleted: 0
- Deleted:  $\leq$
- Deleted:  $\leq$
- Deleted:  $<$
- Deleted:  $<$
- Deleted:  $\leq$
- Deleted: 0.2
- Deleted:  $\leq$
- Deleted:  $\leq$
- Deleted:  $<$
- Deleted:  $<$
- Deleted: (Figs. 6c, f, i).
- Deleted:
- Deleted: one of
- Deleted: dominant factors

- Deleted: 0.2
- Deleted:  $\leq$
- Deleted:  $\leq$
- Deleted:  $<$
- Deleted:  $<$

Formatted: Font: Times New Roman

962 and cloudy-sky conditions, respectively. The near-surface clutter significantly increases  
963 the uncertainty of RWP data, which leads to incapability of analyzing the effect of wind  
964 shear on  $\varepsilon$  below 0.5 km AGL ( $z/z_i \geq 0.3$ ) in the following sections.

965 Regardless of within or above the PBL,  $\varepsilon$  is positively correlated with VWS as shown  
966 in Fig. 7a, d, g and Tabel 2, which indicates that larger VWS leads to stronger turbulence.  
967 This suggests that the dynamic effect of VWS promotes the development of turbulence.  
968 Within the PBL (Figs. 7b, e, h), the slope of  $\varepsilon$  against VWS are smaller than at  $0.3 \leq$   
969  $z/z_i \leq 2.0$  with values ranging from 9.5 to 10.3. Above the PBL (Figs. 7c, f, i), the values  
970 of the slope are larger with values ranging from 10.7 to 18.1, which demonstrating that the  
971 dynamical effects of VWS influence the development of turbulence both within , the upper  
972 PBL and above the PBL.

973 Under cloudy-sky conditions (Figs. 7h, i), the effect of VWS on turbulence within the  
974 upper PBL (Slope=10.3) is weaker than above the PBL (Slope=18.1), significantly.  
975 Compared to the clear-sky conditions (Figs. 7e, f), the values of the slopes are larger for  
976 that of under cloudy-sky conditions (Figs. 7h, i) both within and above the PBL.  
977 Remarkably, above the PBL, the effect of clouds on turbulence is more dramatic, as the  
978 slope value under cloudy-sky conditions is nearly twice as large as that of under clear-sky  
979 conditions. These results indicate the significant mechanical processes driven by VWS is  
980 important in the development of turbulence. A larger VWS in the PBL corresponds to  
981 stronger turbulence. Besides, above the PBL, the mechanical process of VWS is enhanced  
982 under cloudy-sky conditions.

983

### 984 3.2.3. Joint influence of $T_s - T_a$ , VWS and atmosphere stability on $\varepsilon$

985 It was stated that turbulence can be produced by buoyant convective processes (i.e.,  
986 thermals of warm air rising) and by mechanical processes (i.e., wind shear). From the  
987 previous section, it is known that  $T_s - T_a$  and VWS both affect the development of PBL  
988 turbulence. Figure 8 gives the slope profiles of  $\varepsilon$  against  $T_s - T_a$  and VWS at normalized  
989 heights ( $z/z_i$ ) under all-, clear- and cloudy-sky conditions, respectively.

Deleted: 0.2

Deleted:  $\leq$

Deleted:  $\leq$

Deleted: <

Deleted: <

Deleted: and above

Deleted:

Deleted:

998 As inferred from the previous findings,  $T_s - T_a$  primarily influences turbulence  
 999 development within the PBL, irrespective of clear-sky and cloudy-sky conditions (Fig. 6).  
 1000 Figure 8a shows that the slope values within the PBL are predominantly positive, and the  
 1001 slope value decreases rapidly with height, which indicates that the influence of  $T_s - T_a$  on  
 1002 PBL turbulence decreases with height. Interestingly, there is a nearly linear variation of the  
 1003 slope from the lower PBL to the top of the PBL. Within the PBL, the slope is positive,  
 1004 above the PBL, the slope becomes negative. This may be due to the linear decrease of heat  
 1005 flux transport and buoyancy term in the convective PBL (Stull, 1988). Therefore, these  
 1006 findings highlight the predominant thermal forcing of  $T_s - T_a$  on turbulence development  
 1007 within the lower PBL. Fig 8 clearly shows the influence of cloud cover on the  $T_s - T_a$  and  
 1008 the effect of the surface heating on the turbulence in the lower half of the PBL ( $0.3 \leq z/z_i$   
 1009  $\leq 0.5$ ). While there is little difference for the clear-sky and cloudy-sky conditions when  
 1010  $z/z_i > 0.5$ . Hence, under clear-sky conditions, the thermodynamic effect of  $T_s - T_a$  is more  
 1011 pronounced within the lower PBL.

1012 As shown in Fig. 7, it is evident that VWS influences turbulence development within  
 1013 and above the PBL. Figure 8b shows that when  $0.3 < z/z_i \leq 2.0$ , the slope values are  
 1014 consistently positive, indicating that VWS predominantly affects turbulence development  
 1015 within the mid-, upper- PBL and above the PBL. Moreover, when  $0.3 \leq z/z_i \leq 1.2$ , the slope  
 1016 values increase with height. However, when  $1.4 < z/z_i \leq 2.0$ , the slope decreases with height,  
 1017 which suggesting a diminishing influence of VWS. Additionally, within the PBL ( $0.3 \leq$   
 1018  $z/z_i \leq 0.7$ ), the slope values under clear-sky conditions are close to those under cloudy-sky  
 1019 conditions, while the slope values under cloudy-sky conditions are even greater when  
 1020  $0.7 < z/z_i \leq 2.0$ . For instance, when  $z/z_i = 1.4$ ,  $Slope_{Clear-sky} = 14.6$ , while  $Slope_{Cloudy-sky} = 27.0$ ,  
 1021 indicating that the latter is 1.8 times larger than the former. These results suggest that clouds  
 1022 are primarily responsible for enhancing mechanical processes from VWS on turbulence  
 1023 within the upper PBL and above the PBL.

1024 Furthermore, it can be concluded that,  $T_s - T_a$  is the thermodynamic factor influencing  
 1025 turbulence development within the lower PBL ( $0.3 \leq z/z_i \leq 0.5$ ), both  $T_s - T_a$  and VWS  
 1026 jointly strengthen turbulence development in the upper PBL ( $0.6 \leq z/z_i \leq 1.0$ ), and VWS

Deleted: experiences ...creasing...s trend ...ith height. Interestingly, there is a nearly linear variation of the slope from the lower PBL to the top of the PBL. linear of slope value from the lower PBL to a smaller positive value near the top of the PBL... Within the PBL, the slope is positive, A...bove PBL, the slope value ... [47]

Deleted:  $\leq$

Deleted:  $\leq$

Deleted:  $\leq$

Deleted:  $\leq \dots 5$ ). In addition, when  $0.2 < z/z_i < 0.5$ , the slope values are larger for clear-sky conditions than for cloudy-sky conditions, ... [48]

Deleted: w...ile there is little difference for the clear-sky and cloudy-sky conditions when  $0.5 <$  ... [49]

Deleted:  $0.2 \dots 3 \leq$  ... [50]

Deleted:  $<$

Deleted:  $\leq$

Deleted:  $\leq \dots 0$ , the slope values are consistently positive, indicating that VWS predominantly affects turbulence development within the mid-, upper- PBL and above the PBL. Moreover, when  $0.2 \dots 3 \leq$  ... [51]

Deleted:  $\leq$

Deleted:  $<$

Deleted:  $<$

Deleted:  $<$

Deleted:  $\leq$

Deleted:  $\leq \dots 0$ , the slope values exhibit a ...creasing...s trend...ith height, which suggesting a diminishing influence of VWS. Additionally, within the PBL ( $0.2 \dots 3 \leq$  ... [52]

Deleted:  $<$

Deleted:  $<$

Deleted:  $\leq$

Deleted:  $\leq$

Deleted:  $0.2 \dots 3 \leq$  ... [53]

Deleted:  $\leq$

Deleted:  $<$

Deleted:  $<$

Deleted:  $\leq$

Deleted:  $\leq$

Deleted:  $<$

Deleted:  $<$

1114 emerges as the predominant factor affecting turbulence development above the PBL  
1115 ( $1.0 < z/z_i \leq 2.0$ ) (Figs. 8a, b).

1116 The previous sections have revealed that hours of both high  $T_s - T_a$  and strong wind  
1117 shear would strengthen the turbulence within the PBL. Therefore, it's necessary to analyze  
1118 the combined influence of thermodynamics and dynamics factors on the development of  
1119 turbulence. Figure 9 presents the joint distribution of  $\varepsilon$  with  $T_s - T_a$  and VWS within and  
1120 above the PBL under all-, clear- and cloudy-sky conditions. Within the PBL (Figs. 9b, e,  
1121 h), higher  $T_s - T_a$  and VWS correspond to stronger turbulence (Fig. 8). In contrast, the  
1122 thermodynamic effect of  $T_s - T_a$  on turbulence has diminished and is no longer a  
1123 dominant factor above the PBL, while the dynamical effect of VWS becomes the dominant  
1124 factor (Figs. 9c, f, i). Compared to clear-sky conditions, both  $T_s - T_a$  and VWS decrease  
1125 under cloudy-sky conditions (Fig. 9h). This means that the weakening of both  
1126 thermodynamic and dynamic effects leads to a decrease in turbulence, thereby inhibiting  
1127 the development of turbulence within the PBL. Therefore, under cloudy-sky conditions,  
1128 although the VWS is reduced, the dynamical effect of VWS on turbulence is strengthened  
1129 (Figs. 7i and 8b), which in turn strengthens turbulence.

1130 Since buoyant and ~~mechanic~~ forcing jointly influence the turbulence within the PBL,  
1131 and VWS only represents the dynamic driving effect, it cannot accurately portray the effect  
1132 of thermodynamic and dynamic effects on the PBL turbulence. The gradient Richardson  
1133 number ( $Ri$ ), on the other hand, is one of the important parameters characterizing  
1134 atmospheric stability and can compare the buoyant turbulence production term and the  
1135 shear production term in the form of a dimensionless ratio.

1136 Similar to Fig. 9, the joint distribution of  $\varepsilon$  with  $T_s - T_a$  and  $Ri$  within and above the  
1137 PBL under all-sky, clear-sky and cloudy-sky conditions is given in Fig. 10. As shown in  
1138 Fig. 10b, e, h, it is evident that the turbulence in the PBL tend to be enhanced for unstable  
1139 conditions. Furthermore, under clear-sky conditions (Fig. 10e), the maximum number of  
1140 samples is found when  $Ri < 1.0$  and  $T_s - T_a > 21.1$  in strongly unstable conditions, which  
1141 may be caused by the buoyancy forcing driven by the larger  $T_s - T_a$ . By comparison, the  
1142 effect of  $Ri$  on turbulence is relatively weakened above the PBL (Figs. 10c, f, i).  
1143

Deleted: mechanistic

Deleted: Within the PBL (Figs. 10b, e, h),

Deleted: is enhancing

Deleted: While

Deleted: ¶

Deleted: The surface sensible heat flux, boundary layer entrainment energy, VWS, and heat flux at the top of the PBL affected PBL growth. Besides, the cloud top radiative cooling also significantly impacted the PBL development. One main effect of the radiative cooling is the generation of an upward buoyancy flux across the PBL that in turn drives entrainment at the cloud top. Profiles of vertical velocity were found to have enhanced variance under low cumulus compared to clear-sky conditions, suggesting potential for cloud feedbacks on PBL structure and surface energy fluxes (Sedlar et al., 2022).¶

#### 1160 4 Summary and concluding remarks

1161 This study investigates the characteristics of spatio-temporal distribution of daytime  
1162 PBL turbulence dissipation rate ( $\varepsilon$ ) based on more than one-year record (September 2022–  
1163 October 2023) of profiling measurements from a radar wind profilers (RWP) network on  
1164 the Tibet Plateau (TP). Also analyzed are the evolution of  $\varepsilon$  in the PBL and the possible  
1165 influential mechanisms.

1166 First of all,  $\varepsilon$  is firstly retrieved from the vertical wind measurements from RWP using  
1167 the spectral width method. Afterwards, the spatial pattern of  $\varepsilon$  is examined. Results shows  
1168 that the values of  $\varepsilon$  at ~~the~~ Minfeng and Jiuquan ~~stations~~ in the northern TP, and at Dingri  
1169 over the southern TP are about one order of magnitude greater than those at the RWP  
1170 ~~stations~~ of Lijiang, Ganzi and Hongyuan over the eastern TP. Coincidentally, Minfeng and  
1171 Junquan are dominated by bare or semiarid land, as opposed to the highly vegetation-  
1172 covered land surface at Lijiang, Ganzi and Hongyuan. This suggests the spatial discrepancy  
1173 of  $\varepsilon$  over the TP is highly relevant to the types of underlying land cover.

1174 Although  $\varepsilon$  exhibits a variety of magnitudes among the six RWPs, the daytime pattern  
1175 and vertical structure of  $\varepsilon$  are similar. Turbulence reaches the peak in the early afternoon  
1176 (1300–1500 LST), coinciding with the highest PBL top. Under cloudy-sky conditions, the  
1177 daytime mean value of  $\varepsilon$  is  $10^{-4.02} \text{ m}^2 \text{ s}^{-3}$ , and the daytime mean value of the PBL height  
1178 ( $z_i$ ) can reach up to 1.40 km, which is 0.12 km lower than that of clear-sky conditions,  
1179 indicating that clouds would suppress the development of the PBL turbulence.

1180 As far as both the thermodynamic and dynamic forcings are concerned, surface-air  
1181 temperature difference ( $T_s - T_a$ ) and vertical wind shear (VWS) variables are examined by  
1182 performing correlation analysis with  $\varepsilon$ . The slope values of  $\varepsilon$  against  $T_s - T_a$  under clear-  
1183 sky conditions is larger (slope=0.019) than under-cloudy conditions (slope = 0.013) within  
1184 the PBL, while those values are negative above the PBL. The slope values of  $\varepsilon$  against  
1185 VWS ~~are~~ positive regardless of within or above the PBL, where the largest value of 18.1 is  
1186 observed above the PBL under cloudy-sky conditions, and the smallest value of 9.5 is  
1187 observed in the PBL ~~under~~ clear-sky conditions.

Deleted: both

Deleted: site

Deleted: site

Formatted: Font: (Default) Times New Roman

Formatted: Font: Times New Roman

Deleted: 415

Deleted: 117

Deleted: is

Deleted: within

Deleted: in



1196 Both the thermodynamic effect of  $T_s - T_a$  and the dynamic effect of VWS enhance the  
 1197 development of turbulence under clear-sky or cloudy-sky conditions in the PBL. In the  
 1198 lower PBL ( $0.3 \leq z/z_i \leq 0.5$ ),  $T_s - T_a$  has a larger positive slope with  $\epsilon$ , which suggests  
 1199 that thermal forcing emerges as the dominant factor influencing development of the  
 1200 turbulence and PBL. By comparison, in the upper PBL ( $0.6 \leq z/z_i \leq 1.0$ ),  $T_s - T_a$  and VWS  
 1201 jointly influence the development of turbulence, with larger  $T_s - T_a$  leading to unstable  
 1202 atmospheric stability and stronger turbulence. Above the PBL ( $1.0 < z/z_i \leq 2.0$ ), VWS  
 1203 becomes the dominant factor influencing the development of turbulence. Compared to  
 1204 clear-sky conditions, on one hand, clouds would diminish  $T_s - T_a$ , resulting in decreased  
 1205 heat transfer from the surface to the PBL top, thereby weakening turbulence within the  
 1206 lower PBL ( $0.3 \leq z/z_i \leq 0.5$ ), inhibiting PBL development, and decreasing  $z_i$ . On the other  
 1207 hand, the stronger wind shear process would enhance the turbulence above PBL under the  
 1208 cloudy-sky conditions.

1209 Although the above-mentioned findings of the PBL turbulence over the TP are the first  
 1210 results from profiling network observations to the best of our knowledge, fine-resolution  
 1211 spatial distribution remains unclear, largely due to the sparse distribution of RWP network  
 1212 on the TP. On top of this, the role of roughness length, vertical velocity, and entrainment  
 1213 remains unknown in the variation and evolution of atmospheric turbulence, which warrants  
 1214 further in-depth studies based on intensive field campaigns, in combination with theoretical  
 1215 analysis and numerical simulation experiments in the future.

1217 **Data Availability**

1218 The authors would like to acknowledge the National Meteorological Information Centre  
 1219 (NMIC) of China Meteorological Administration (CMA) (<https://data.cma.cn>) for  
 1220 providing the high-resolution radar wind profiler and ground-based meteorological data,  
 1221 which can be only accessed via registration. We are grateful to ECMWF for providing  
 1222 ERA5 hourly data (<https://www.ecmwf.int/en/forecasts/datasets/reanalysis-datasets/era5/>).

Deleted: 0.2  
 Deleted:  $\leq$   
 Deleted:  $\leq$   
 Deleted:  $<$   
 Deleted:  $<$   
 Deleted:  $\leq$   
 Deleted:  $<$   
 Deleted:  $<$

Deleted: 0.2  
 Deleted:  $\leq$   
 Deleted:  $\leq$   
 Deleted:  $<$   
 Deleted:  $<$

Deleted: , especially in the lowest part of PBL

Deleted: a field campaign involved in the high-density turbulence observation network along with high-resolution satellite images

Field Code Changed

Field Code Changed



1241 **Acknowledgments**

1242 This work was jointly supported by the National Natural Science Foundation of China  
1243 under grant 42325501, the High Impact Weather Key Laboratory of CMA, and NSFC  
1244 under grants U2142209 and 42105090, the China Meteorological Administration Xiong'an  
1245 Atmospheric Boundary Layer Key Laboratory under grant 2023LABL-B06, and Chinese  
1246 Academy of Meteorological Sciences under grants 2021KJ008 and 2024Z003. Last but not  
1247 least, we appreciated tremendously the constructive comments and suggestions made by  
1248 the anonymous reviewers that significantly improved the quality of our manuscript.

1249 **Author Contributions**

1250 The study was completed with close cooperation between all authors. JG and XG conceived  
1251 of the idea for this work. DM performed the analysis, DM and JG drafted the original  
1252 manuscript with contributions from XG, NL, YS, ZZ and NT. YW, HL, FZ, BT, HX and  
1253 TC provided useful suggestions and comments for the study and helped revise the  
1254 manuscript.

1255 **Completing interests**

1256 The authors declare that they have no conflict of interest.

1257 **References**

1258 Adler, B. and Kalthoff, N.: Multi-scale transport processes observed in the boundary layer  
1259 over a mountainous island, Bound.-Layer Meteor., 153, 515-537,  
1260 <https://doi.org/10.1007/s10546-014-9957-8>, 2014.  
1261 [Angel A C, Manoj M G. A novel method of estimating atmospheric boundary layer height](#)  
1262 [using a 205 MHz VHF radar. Sci. Total. Environ.,](#)  
1263 <https://doi.org/10.1016/j.scitotenv.2023.168109, 907: 168109, 2024,>  
1264 Banerjee, T., Brugger, P., De Roo, F., Kröniger, K., Yakir, D., Rotenberg, E., and Mauder,  
1265 M.: Turbulent transport of energy across a forest and a semiarid shrubland, Atmos.  
1266 Chem. Phys., 18, 10025–10038, <https://doi.org/10.5194/acp-18-10025-2018>, 2018.

Deleted: s

Deleted: ,

Formatted: Font: (Default) Times New Roman, (Asian) Times New Roman, 12 pt, Font colour: Text 1, English (US)

Formatted: Font: (Default) Times New Roman, (Asian) Times New Roman, 12 pt, Font colour: Text 1, English (US)

Deleted:

Moved (insertion) [3]

Formatted: Font: (Asian) Times New Roman, Font colour: Text 1, Not Highlight

Deleted: (

Formatted: Font: (Asian) Times New Roman, Font colour: Text 1

Deleted: (No.

Deleted: ) ¶

Formatted: Font colour: Text 1

Moved up [3]: (China Meteorological Administration Xiong'an Atmospheric Boundary Layer Key Laboratory (No. 2023LABL-B06) ¶

Formatted: Highlight

Formatted: Font: Not Bold, Highlight

Formatted: Highlight

Formatted: Font: Not Bold, Highlight

Formatted: Font: (Asian) +Body Asian (DengXian)

Formatted: Font: Not Italic

Formatted: Font: (Asian) +Body Asian (DengXian)

1276 Bianco, L., Wilczak, J. M., and White, A. B.: Convective boundary layer depth estimation  
1277 from wind profilers: Statistical comparison between an automated algorithm and  
1278 expert estimations, *J. Atmos. Ocean. Technol.*, 25, 1397-1413,  
1279 <https://doi.org/10.1175/2008jtecha981.1>, 2008.

1280 Bodenschatz, E., Malinowski, S. P., Shaw, R. A., and Stratmann, F.: Can we understand  
1281 clouds without turbulence? *Science*, 327, 970-971,  
1282 <https://doi.org/10.1126/science.1185138>, 2010.

1283 Che, J. H. and Zhao, P.: Characteristics of the summer atmospheric boundary layer height  
1284 over the Tibetan Plateau and influential factors, *Atmos. Chem. Phys.*, 21, 5253-5268,  
1285 <https://doi.org/10.5194/acp-21-5253-2021>, 2021.

1286 Chechin, D. G., Lüpkes, C., Hartmann, J., Ehrlich, A., and Wendisch, M.: Turbulent  
1287 structure of the Arctic boundary layer in early summer driven by stability, wind shear  
1288 and cloud-top radiative cooling: ACLOUD airborne observations, *Atmos. Chem.*  
1289 *Phys.*, 23, 4685-4707, <https://doi.org/10.5194/acp-23-4685-2023>, 2023.

1290 Chen, X. L., Añel, J. A., Su, Z. B., de la Torre, L., Kelder, H., van Peet, J., and Ma, Y. M.:  
1291 The deep atmospheric boundary layer and its significance to the stratosphere and  
1292 troposphere exchange over the Tibetan Plateau, *PLoS One*, 8, 9,  
1293 <https://doi.org/10.1371/journal.pone.0056909>, 2013.

1294 Chen, X. L., Skerlak, B., Rotach, M. W., Añel, J. A., Su, Z., Ma, Y. M., and Li, M. S.:  
1295 Reasons for the extremely high-ranging planetary boundary layer over the western  
1296 Tibetan Plateau in winter, *J. Atmos. Sci.*, 73, 2021-2038, [https://doi.org/10.1175/jas-](https://doi.org/10.1175/jas-d-15-0148.1)  
1297 [d-15-0148.1](https://doi.org/10.1175/jas-d-15-0148.1), 2016.

1298 Chen, Z., Tian, Y., Wang, Y., Bi, Y., Wu, X., Huo, J., Pan, L., Wang, Y., and Lü, D.:  
1299 Turbulence parameters measured by the Beijing mesosphere-stratosphere-  
1300 troposphere radar in the troposphere and lower stratosphere with three models:  
1301 comparison and analyses, *Atmos. Meas. Tech.*, 15, 4785-4800,  
1302 <https://doi.org/10.5194/amt-15-4785-2022>, 2022.

1303 Collaud Coen, M., Praz, C., Haeefe, A., Ruffieux, D., Kaufmann, P., and Calpini, B.:  
1304 Determination and climatology of the planetary boundary layer height above the  
1305 Swiss plateau by in situ and remote sensing measurements as well as by the COSMO-

Formatted: Font: Not Italic

Formatted: Font: Not Italic

Formatted: Default Paragraph Font, Font: Not Italic, Font colour: Text 1

Formatted: Font: Not Italic

1306 [2 model, Atmos. Chem. Phys., 14, 13205–13221, https://doi.org/10.5194/acp-14-](https://doi.org/10.5194/acp-14-13205-2014)  
1307 [13205-2014, 2014.](https://doi.org/10.5194/acp-14-13205-2014)

1308 Dai, C., Wang, Q., Kalogiros, J. A., Lenschow, D. H., Gao, Z., and Zhou, M.: Determining  
1309 boundary-layer height from aircraft measurements, *Bound.-Layer Meteor.*, 152, 277-  
1310 302, <https://doi.org/10.1007/s10546-014-9929-z>, 2014.

1311 [Davis E V, Rajeev K, and Mishra M K: Effect of clouds on the diurnal evolution of the](https://doi.org/10.1007/s10546-019-00497-6)  
1312 [atmospheric boundary-layer height over a tropical coastal station. \*Bound.-Layer\*](https://doi.org/10.1007/s10546-019-00497-6)  
1313 [Meteor., 175: 135-152, https://doi.org/10.1007/s10546-019-00497-6, 2020.](https://doi.org/10.1007/s10546-019-00497-6)

1314 Dodson, D. S. and Griswold, J. D. S.: Turbulent and boundary layer characteristics during  
1315 VOCALS-REx, *Atmos. Chem. Phys.*, 21, 1937-1961, [https://doi.org/10.5194/acp-21-](https://doi.org/10.5194/acp-21-1937-2021)  
1316 [1937-2021, 2021.](https://doi.org/10.5194/acp-21-1937-2021)

1317 [Duncan Jr., J. B., Bianco, L., Adler, B., Bell, T., Djalalova, I. V., Riihimaki, L., Sedlar, J.,](https://doi.org/10.5194/amt-15-2479-2022)  
1318 [Smith, E. N., Turner, D. D., Wagner, T. J., and Wilczak, J. M.: Evaluating convective](https://doi.org/10.5194/amt-15-2479-2022)  
1319 [planetary boundary layer height estimations resolved by both active and passive](https://doi.org/10.5194/amt-15-2479-2022)  
1320 [remote sensing instruments during the CHEESEHEAD19 field campaign, \*Atmos.\*](https://doi.org/10.5194/amt-15-2479-2022)  
1321 [Meas. Tech., 15, 2479–2502, https://doi.org/10.5194/amt-15-2479-2022, 2022.](https://doi.org/10.5194/amt-15-2479-2022)

1322 Guo, J. P., Li, Y., Cohen, J. B., Li, J., Chen, D. D., Xu, H., Liu, L., Yin, J. F., Hu, K. X.,  
1323 and Zhai, P. M.: Shift in the temporal trend of boundary layer height in China using  
1324 long-term (1979-2016) radiosonde data, *Geophys. Res. Lett.*, 46, 6080-6089,  
1325 <https://doi.org/10.1029/2019gl082666>, 2019.

1326 Guo, J. P., Miao, Y. C., Zhang, Y., Liu, H., Li, Z. Q., Zhang, W. C., He, J., Lou, M. Y.,  
1327 Yan, Y., Bian, L. G., and Zhai, P.: The climatology of planetary boundary layer height  
1328 in China derived from radiosonde and reanalysis data, *Atmos. Chem. Phys.*, 16,  
1329 13309-13319, <https://doi.org/10.5194/acp-16-13309-2016>, 2016.

1330 Guo, J. P., Liu, B. M., Gong, W., Shi, L. J., Zhang, Y., Ma, Y. Y., Zhang, J., Chen, T. M.,  
1331 Bai, K. X., Stoffelen, A., de Leeuw, G., and Xu, X. F.: First comparison of wind  
1332 observations from ESA's satellite mission Aeolus and ground-based radar wind  
1333 profiler network of China, *Atmos. Chem. Phys.*, 21, 2945-2958,  
1334 <https://doi.org/10.5194/acp-21-2945-2021>, 2021a.

1335 Guo, J. P., Zhang, J., Yang, K., Liao, H., Zhang, S. D., Huang, K. M., Lv, Y. M., Shao, J.,  
1336 Yu, T., Tong, B., Li, J., Su, T. N., Yim, S. H. L., Stoffelen, A., Zhai, P. M., and Xu,

1337 X. F.: Investigation of near-global daytime boundary layer height using high-  
1338 resolution radiosondes: first results and comparison with ERA5, MERRA-2, JRA-55,  
1339 and NCEP-2 reanalyses, *Atmos. Chem. Phys.*, 21, 17079-17097,  
1340 <https://doi.org/10.5194/acp-21-17079-2021>, 2021b.

1341 Guo, X. R., Guo, J. P., Zhang, D. L., and Yun, Y. X.: Vertical divergence profiles as  
1342 detected by two wind-profiler mesonets over East China: Implications for nowcasting  
1343 convective storms, *Q. J. R. Meteorol. Soc.*, 149, 1629-1649,  
1344 <https://doi.org/10.1002/qj.4474>, 2023.

1345 Hersbach, H., Bell, B., Berrisford, P., Hirahara, S., Horányi, A., Muñoz-Sabater, J., Nicolas,  
1346 J., Peubey, C., Radu, R., Schepers, D., Simmons, A., Soci, C., Abdalla, S., Abellan,  
1347 X., Balsamo, G., Bechtold, P., Biavati, G., Bidlot, J., Bonavita, M., De Chiara, G.,  
1348 Dahlgren, P., Dee, D., Diamantakis, M., Dragani, R., Flemming, J., Forbes, R.,  
1349 Fuentes, M., Geer, A., Haimberger, L., Healy, S., Hogan, R. J., Hólm, E., Janisková,  
1350 M., Keeley, S., Laloyaux, P., Lopez, P., Lupu, C., Radnoti, G., de Rosnay, P., Rozum,  
1351 I., Vamborg, F., Villaume, S., and Thépaut, J. N.: The ERA5 global reanalysis, *Q. J.  
1352 R. Meteorol. Soc.*, 146, 1999-2049, <https://doi.org/10.1002/qj.3803>, 2020.

1353 Huang, J. P., Zhou, X. J., Wu, G. X., Xu, X. D., Zhao, Q. Y., Liu, Y. M., Duan, A. M., Xie,  
1354 Y. K., Ma, Y. M., Zhao, P., Yang, S., Yang, K., Yang, H. J., Bian, J. C., Fu, Y. F., Ge,  
1355 J. M., Liu, Y. Z., Wu, Q. G., Yu, H. P., Wang, B. B., Bao, Q., and Qie, K.: Global  
1356 climate impacts of land-surface and atmospheric processes over the Tibetan Plateau,  
1357 *Rev. Geophys.*, 61, 39, <https://doi.org/10.1029/2022rg000771>, 2023.

1358 [Huang, T., Yim, S. H. L., Yang, Y., Lee, O. S. M., Lam, D. H. Y., Cheng, J. C. H., and](#)  
1359 [Guo, J.: Observation of turbulent mixing characteristics in the typical daytime cloud-](#)  
1360 [topped boundary layer over Hong Kong in 2019, \*Remote Sens.\*, 12, 1533,](#)  
1361 <https://doi.org/10.3390/RS12091533>, 2020.

1362 Jacoby-Koaly, S., Campistron, B., Bernard, S., Bénech, B., Girard-Ardhuin, F., Dessens,  
1363 J., Dupont, E., and Carissimo, B.: Turbulent dissipation rate in the boundary layer via  
1364 UHF wind profiler Doppler spectral width measurements, *Bound.-Layer Meteor.*, 103,  
1365 361-389, <https://doi.org/10.1023/a:1014985111855>, 2002.

1366 Kotthaus, S., Bravo-Aranda, J. A., Coen, M. C., Guerrero-Rascado, J. L., Costa, M. J.,  
1367 Cimini, D., O'Connor, E. J., Hervo, M., Alados-Arboledas, L., Jiménez-Portaz, M.,

1368 Mona, L., Ruffieux, D., Illingworth, A., and Haeffelin, M.: Atmospheric boundary  
1369 layer height from ground-based remote sensing: a review of capabilities and  
1370 limitations, *Atmos. Meas. Tech.*, 16, 433-479, [https://doi.org/10.5194/amt-16-433-](https://doi.org/10.5194/amt-16-433-2023)  
1371 2023, 2023.

1372 Lai, Y., Chen, X. L., Ma, Y. M., Chen, D. L., and Zhaxi, S. L.: Impacts of the westerlies  
1373 on planetary boundary layer growth over a valley on the north side of the Central  
1374 Himalayas, *J. Geophys. Res.-Atmos.*, 126, 20, <https://doi.org/10.1029/2020jd033928>,  
1375 2021.

1376 Li, Y., Y. Wu, J. Tang, P. Zhu, Z. Gao, and Y. Yang. Quantitative evaluation of wavelet  
1377 analysis method for turbulent flux calculation of non-stationary series, *Geophys. Res.*  
1378 *Lett.*, 50(5), e2022GL101591, <http://dx.doi.org/10.1029/2022GL101591>, 2023.

1379 Li, Z. G., Lyu, S. H., Wen, L. J., Zhao, L., Ao, Y. H., and Wang, S. Y.: Effect of a cold,  
1380 dry air incursion on atmospheric boundary layer processes over a high-altitude lake in  
1381 the Tibetan Plateau, *Atmos. Res.*, 185, 32-43,  
1382 <https://doi.org/10.1016/j.atmosres.2016.10.024>, 2017a.

1383 Li, Z. Q., Guo, J. P., Ding, A. J., Liao, H., Liu, J. J., Sun, Y. L., Wang, T. J., Xue, H. W.,  
1384 Zhang, H. S., and Zhu, B.: Aerosol and boundary-layer interactions and impact on air  
1385 quality, *Natl. Sci. Rev.*, 4, 810-833, <https://doi.org/10.1016/10.1093/nsr/nwx117>,  
1386 2017b.

1387 Liu, B. M., Guo, J. P., Gong, W., Shi, L. J., Zhang, Y., and Ma, Y. Y.: Characteristics and  
1388 performance of wind profiles as observed by the radar wind profiler network of China,  
1389 *Atmos. Meas. Tech.*, 13, 4589-4600, <https://doi.org/10.5194/amt-13-4589-2020>, 2020.

1390 Liu, B. M., Ma, Y. Y., Guo, J. P., Gong, W., Zhang, Y., Mao, F. Y., Li, J., Guo, X. R., and  
1391 Shi, Y. F.: Boundary layer heights as derived from ground-based radar wind profiler  
1392 in Beijing, *IEEE Trans. Geosci. Remote Sensing*, 57, 8095-8104,  
1393 <https://doi.org/10.1109/tgrs.2019.2918301>, 2019.

1394 Lv, Y. M., Guo, J. P., Li, J., Cao, L. J., Chen, T. M., Wang, D., Chen, D. D., Han, Y., Guo,  
1395 X. R., Xu, H., Liu, L., Solanki, R., and Huang, G.: Spatiotemporal characteristics of  
1396 atmospheric turbulence over China estimated using operational high-resolution  
1397 soundings, *Environ. Res. Lett.*, 16, 13, <https://doi.org/10.1088/1748-9326/abf461>,  
1398 2021.

Field Code Changed

1399 Ma, Y. M., Yao, T. D., Zhong, L., Wang, B. B., Xu, X. D., Hu, Z. Y., Ma, W. Q., Sun, F.  
1400 L., Han, C. B., Li, M. S., Chen, X. L., Wang, J. M., Li, Y. Q., Gu, L. L., Xie, Z. P.,  
1401 Liu, L., Sun, G. H., Wang, S. J., Zhou, D. G., Zuo, H. C., Xu, C., Liu, X., Wang, Y.  
1402 J., and Wang, Z. Y.: Comprehensive study of energy and water exchange over the  
1403 Tibetan Plateau: A review and perspective: From GAME/Tibet and CAMP/Tibet to  
1404 TORP, TPEORP, and TPEITORP, *Earth-Sci. Rev.*, 104312, 2023.

1405 McCaffrey, K., Bianco, L., and Wilczak, J. M.: Improved observations of turbulence  
1406 dissipation rates from wind profiling radars, *Atmos. Meas. Tech.*, 10, 2595-2611,  
1407 <https://doi.org/10.5194/amt-10-2595-2017>, 2017.

1408 Muhsin, M., Sunilkumar, S. V., Ratnam, M. V., Parameswaran, K., Murthy, B. V. K.,  
1409 Ramkumar, G., and Rajeev, K.: Diurnal variation of atmospheric stability and  
1410 turbulence during different seasons in the troposphere and lower stratosphere derived  
1411 from simultaneous radiosonde observations at two tropical stations, in the Indian  
1412 Peninsula, *Atmos. Res.*, 180, 12-23, <https://doi.org/10.1016/j.atmosres.2016.04.021>,  
1413 2016.

1414 Muñoz-Esparza, D., Sharman, R. D., and Lundquist, J. K.: Turbulence Dissipation Rate in  
1415 the Atmospheric Boundary Layer: Observations and WRF Mesoscale Modeling  
1416 during the XPIA Field Campaign, *Mon. Weather Rev.*, 146, 351-371,  
1417 <https://doi.org/10.1175/mwr-d-17-0186.1>, 2018.

1418 Nastrom, G. D.: Doppler radar spectral width broadening due to beamwidth and wind shear,  
1419 *Ann. Geophys.-Atmos. Hydrospheres Space Sci.*, 15, 786-796,  
1420 <https://doi.org/10.1007/s00585-997-0786-7>, 1997.

1421 [Nicholls, S.: The dynamics of stratocumulus: Aircraft observations and comparisons with](#)  
1422 [a mixed layer model, \*Q. J. Roy. Meteor. Soc.\*, 110, 783–820,](#)  
1423 <https://doi.org/10.1002/qj.49711046603>, 1984.

1424 Ruan, Z., Mu, R. Q., Wei, M., and Ge, R. S.: Spectrum analysis of wind profiling radar  
1425 measurements, *J. Meteorol. Res.*, 28, 656-667, [https://doi.org/10.1007/s13351-014-](https://doi.org/10.1007/s13351-014-3171-y)  
1426 [3171-y](https://doi.org/10.1007/s13351-014-3171-y), 2014.

1427 [Sedlar, J., Riihimaki, L. D., Turner, D. D., Duncan, J., Adler, B., Bianco, L., Lantz, K., and](#)  
1428 [Wilczak, J.: Investigating the impacts of daytime boundary layer clouds on surface](#)

1429 [energy fluxes and boundary layer structure during CHEESEHEAD19](#), *J. Geophys.*  
1430 *Res.-Atmos.*, 127, e2021JD036060, <https://doi.org/10.1029/2021JD036060>, 2022

1431 Schumann, U. and Moeng, C. H.: Plume budgets in clear and cloudy convective boundary  
1432 layers, *J. Atmos. Sci.*, 48, 1758-1770, <https://doi.org/10.1175/1520->  
1433 0469(1991)048<1758:Pbicac>2.0.Co;2, 1991.

1434 Slättberg, N., Lai, H. W., Chen, X. L., Ma, Y. M., and Chen, D. L.: Spatial and temporal  
1435 patterns of planetary boundary layer height during 1979-2018 over the Tibetan Plateau  
1436 using ERA5, *Int. J. Climatol.*, 42, 3360-3377, <https://doi.org/10.1002/joc.7420>, 2022.

1437 Solanki, R., Guo, J. P., Lv, Y. M., Zhang, J., Wu, J. Y., Tong, B., and Li, J.: Elucidating  
1438 the atmospheric boundary layer turbulence by combining UHF radar wind profiler  
1439 and radiosonde measurements over urban area of Beijing, *Urban CLim.*, 43, 13,  
1440 <https://doi.org/10.1016/j.uclim.2022.101151>, 2022.

1441 Solanki, R., Guo, J. P., Li, J., Singh, N., Guo, X. R., Han, Y., Lv, Y. M., Zhang, J., and Liu,  
1442 B. M.: Atmospheric-boundary-layer-height variation over mountainous and urban  
1443 [stations](#) in Beijing as derived from radar wind-profiler measurements, *Bound.-Layer*  
1444 *Meteor.*, 181, 125-144, <https://doi.org/10.1007/s10546-021-00639-9>, 2021.

1445 Stull, R. B.: Mean Boundary Layer Characteristics, in: *An Introduction to boundary layer*  
1446 *meteorology*, edited by: Stull, R. B., Springer Netherlands, Dordrecht, 1–27,  
1447 [https://doi.org/10.1007/978-94-009-3027-8\\_1](https://doi.org/10.1007/978-94-009-3027-8_1), 1988. \_

1448 [Su, T. N., Li, Z. Q., and Zheng, Y. T.: Cloud-Surface Coupling Alters the Morning](#)  
1449 [Transition From Stable to Unstable Boundary Layer](#), *Geophys. Res. Lett.*, 50, 9,  
1450 <https://doi.org/10.1029/2022gl102256>, 2023.\_

1451 [Sun, W., Li, L., and Wang, B.: Reducing the biases in shortwave cloud radiative forcing in](#)  
1452 [tropical and subtropical regions from the perspective of boundary layer processes](#), *Sci.*  
1453 *China Earth Sci.*, 59, 1427–1439, <https://doi.org/10.1007/s11430-016-5290-z>, 2016.

1454 Teixeira, J., Piepmeier, J. R., Nehrir, A. R., Ao, C. O., Chen, S. S., Clayson, C. A., Fridlind,  
1455 A. M., Lebsock, M., McCarty, W., Salmun, H., Santanello, J. A., Turner, D. D., Wang,  
1456 Z., and Zeng, X.: Toward a global planetary boundary layer observing system: the  
1457 NASA PBL incubation study team report, NASA PBL Incubation Study Team, 134  
1458 pp., available at: <https://science.nasa.gov/science-red/s3fs->

Deleted: site

1460 public/atoms/files/NASAPBLIncubationFinalReport.pdf, last access: 15 November  
1461 2021.

1462 Wan, X., Zheng, J. F., Wan, R., Xu, G. R., Qin, J. F., and Yi, L.: Intercomparison of cloud  
1463 vertical structures over four different ~~stations~~ of the eastern slope of the Tibetan  
1464 Plateau in summer using Ka-band millimeter-wave radar measurements, *Remote*  
1465 *Sens.*, 14, 19, <https://doi.org/10.3390/rs14153702>, 2022.

1466 Wang, C. X., Ma, Y. M., and Han, C. B.: Research on the atmospheric boundary layer  
1467 structure and its development mechanism in the Tibetan Plateau, *Adv. Atmos. Sci.*,  
1468 38, 414-428, 2023a.

1469 Wang, M. Z. and Zhang, J. T.: The relationship among summer atmospheric boundary layer  
1470 height over the Taklimakan Desert, its land surface parameters and Eurasian  
1471 circulation, *Atmos. Sci. Lett.*, 23, 13, <https://doi.org/10.1002/asl.1122>, 2022.

1472 Wang, M. Z., Lu, H., Ming, H., and Zhang, J. T.: Vertical structure of summer clear-sky  
1473 atmospheric boundary layer over the hinterland and southern margin of Taklamakan  
1474 Desert, *Meteorol. Appl.*, 23, 438-447, <https://doi.org/10.1002/met.1568>, 2016.

1475 Wang, S. Q., Guo, J. P., Xian, T., Li, N., Meng, D. L., Li, H. J., and Cheng, W.:  
1476 Investigation of low-level supergeostrophic wind and Ekman spiral as observed by a  
1477 radar wind profiler in Beijing, *Front. Environ. Sci.*, 11, 9,  
1478 <https://doi.org/10.3389/fenvs.2023.1195750>, 2023b.

1479 Wang, Y. J., Zeng, X. B., Xu, X. D., Xie, F. Q., and Zhao, Y.: Improving the estimate of  
1480 summer daytime planetary boundary layer height over land from GPS radio  
1481 occultation data, *Geophys. Res. Lett.*, 49, 9, <https://doi.org/10.1029/2021gl096304>,  
1482 2022.

1483 Wang, Y. J., Xu, X. D., Zhao, T. L., Sun, J. H., Yao, W. Q., and Zhou, M. Y.: Structures  
1484 of convection and turbulent kinetic energy in boundary layer over the southeastern  
1485 edge of the Tibetan Plateau, *Sci. China-Earth Sci.*, 58, 1198-1209,  
1486 <https://doi.org/10.1007/s11430-015-5054-1>, 2015.

1487 Wang, Y. J., Zeng, X. B., Xu, X. D., Welty, J., Lenschow, D. H., Zhou, M. Y., and Zhao,  
1488 Y.: Why are there more summer afternoon low clouds over the Tibetan Plateau  
1489 compared to eastern China? *Geophys. Res. Lett.*, 47, 10,  
1490 <https://doi.org/10.1029/2020gl089665>, 2020.

Deleted: site



1492 White, A. B., Lataitis, R. J., and Lawrence, R. S.: Space and time filtering of remotely  
1493 sensed velocity turbulence, *J. Atmos. Ocean. Technol.*, 16, 1967-1972,  
1494 [https://doi.org/10.1175/1520-0426\(1999\)016<1967:Satfor>2.0.Co;2](https://doi.org/10.1175/1520-0426(1999)016<1967:Satfor>2.0.Co;2), 1999.

1495 Wu, J. Y., Guo, J. P., Yun, Y. X., Yang, R. F., Guo, X. R., Meng, D. L., Sun, Y. P., Zhang,  
1496 Z., Xu, H., and Chen, T. M.: Can ERA5 reanalysis data characterize the pre-storm  
1497 environment? *Atmos. Res.*, 297, 18, <https://doi.org/10.1016/j.atmosres.2023.107108>,  
1498 2024.

1499 Xu, L. J., Liu, H. Z., Du, Q., and Xu, X. D.: The assessment of the planetary boundary  
1500 layer schemes in WRF over the central Tibetan Plateau, *Atmos. Res.*, 230, 12,  
1501 <https://doi.org/10.1016/j.atmosres.2019.104644>, 2019.

1502 Xu, X. D., Tang, Y., Wang, Y. J., Zhang, H. S., Liu, R. X., and Zhou, M. Y.: Triggering  
1503 effects of large topography and boundary layer turbulence on convection over the  
1504 Tibetan Plateau, *Atmos. Chem. Phys.*, 23, 3299-3309, <https://doi.org/10.5194/acp-23-3299-2023>, 2023.

1506 Xu, X. D., Zhou, M. Y., Chen, J. Y., Bian, L. G., Zhang, G. Z., Liu, H. Z., Li, S. M., Zhang,  
1507 H. S., Zhao, Y. J., Suolong, D.J., and Wang, J. Z.: A comprehensive physical pattern  
1508 of land-air dynamic and thermal structure on the Qinghai-Xizang Plateau, *Sci. China  
1509 Ser. D-Earth Sci.*, 45, 577-594, <https://doi.org/10.1360/02yd9060>, 2002.

1510 Yang, B., Qian, Y., Berg, L. K., Ma, P. L., Wharton, S., Bulaevskaya, V., Yan, H. P., Hou,  
1511 Z. S., and Shaw, W. J.: Sensitivity of Turbine-Height Wind Speeds to Parameters in  
1512 Planetary Boundary-Layer and Surface-Layer Schemes in the Weather Research and  
1513 Forecasting Model, *Bound.-Layer Meteor.*, 162, 117-142,  
1514 <https://doi.org/10.1007/s10546-016-0185-2>, 2017.

1515 Yang, R. F., Guo, J. P., Deng, W. L., Li, N., Fan, J. H., Meng, D. L., Liu, Z., Sun, Y. P.,  
1516 Zhang, G. L., and Liu, L. H.: Investigation of turbulent dissipation rate profiles from  
1517 two radar wind profilers at plateau and plain stations in the north China plain, *Remote  
1518 Sens.*, 15, 14, <https://doi.org/10.3390/rs15164103>, 2023.

1519 Zhang, L., Zhang, H. S., Li, Q. H., Wei, W., Cai, X. H., Song, Y., Mamtimin, A., Wang,  
1520 M. Z., Yang, F., Wang, Y., and Zhou, C. L.: Turbulent mechanisms for the deep  
1521 convective boundary layer in the Taklimakan desert, *Geophys. Res. Lett.*, 49, 9,  
1522 <https://doi.org/10.1029/2022gl099447>, 2022.

1523 Zhang, Y., Guo, J. P., Yang, Y. J., Wang, Y., and Yim, S. H. L.: Vertica wind shear  
1524 modulates particulate matter pollutions: a perspective from radar wind profiler  
1525 observations in Beijing, China, *Remote Sens.*, 12, 17,  
1526 <https://doi.org/10.3390/rs12030546>, 2020.

1527 Zhao, P., Li, Y. Q., Guo, X. L., Xu, X. D., Liu, Y. M., Tang, S. H., Xiao, W. M., Shi, C.  
1528 X., Ma, Y. M., Yu, X., Liu, H. Z., Jia, L., Chen, Y., Liu, Y. J., Li, J., Luo, D. B., Cao,  
1529 Y. C., Zheng, X. D., Chen, J. M., Xiao, A., Yuan, F., Chen, D. H., Pang, Y., Hu, Z.  
1530 Q., Zhang, S. J., Dong, L. X., Hu, J. Y., Han, S., and Zhou, X. J.: The Tibetan Plateau  
1531 surface-atmosphere coupling system and its weather and climate effects: the third  
1532 Tibetan Plateau atmospheric science experiment, *J. Meteorol. Res.*, 33, 375-399,  
1533 <https://doi.org/10.1007/s13351-019-8602-3>, 2019.

1534

1535 **Table list**

1536 **Table 1.** Summary of the geographical conditions and land surface of the six radar wind  
1537 profiler (RWP) stations over the Tibet Plateau (TP).

RWP station	Latitude (°E)	Longitude (°N)	Elevation (m)	Land cover types
Minfeng	82.69	37.07	1408.9	Bare land
Jiuquan	98.49	39.77	1477.2	Bare land
Dingri	87.07	28.39	4326.0	Grassland
Ganzi	100.00	31.62	3353.0	Bare land, grassland
Hongyuan	102.55	32.79	3465.0	Bare land, grassland
Lijiang	100.22	26.85	2382.4	Bare land, grass land

Deleted: site

Deleted: site

1538

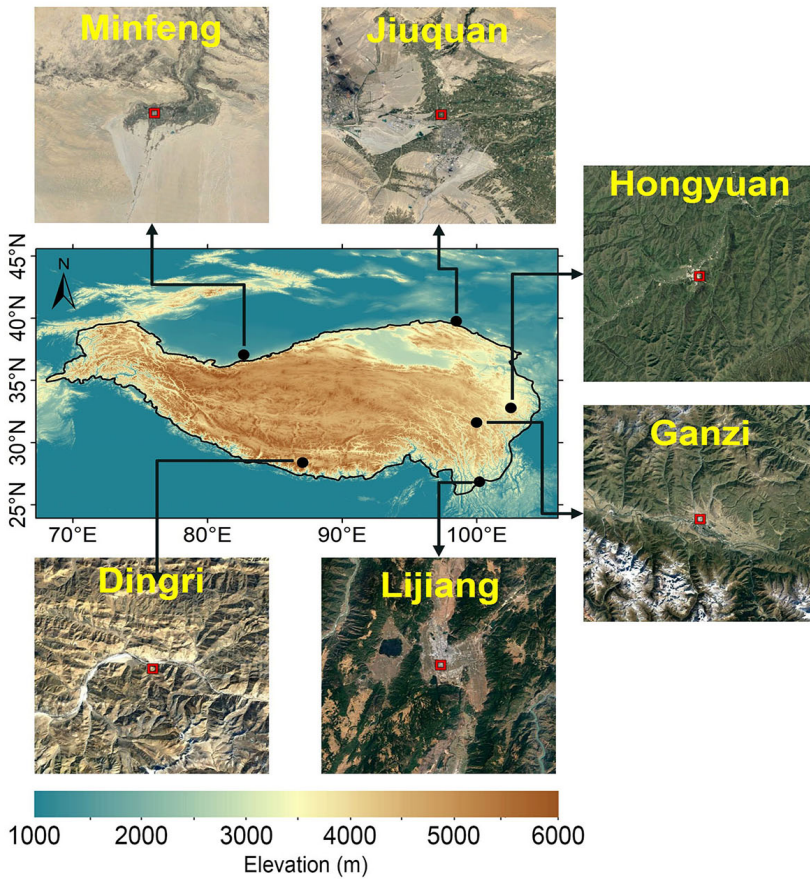
1539

1542 **Table 2.** Summary of the correlation of  $\text{Log}_{10}\epsilon$  at different altitude ranges under all-,  
 1543 clear- and cloudy-sky conditions with  $T_s - T_a$  and vertical wind shear (VWS) for all six  
 1544 RWP Stations. The superscript \* for R indicates that the regression slope is statistically  
 1545 significant at  $p < 0.01$ .

Conditions	$\text{Log}_{10}\epsilon$ VS $T_s - T_a$	$\text{Log}_{10}\epsilon$ VS VWS
all-sky, $0.3 \leq z/z_i \leq 2.0$	$y=0.010x-4.05$ , R=0.21*	$y=13.6x-4.19$ , R=0.29*
all-sky, $0.3 \leq z/z_i \leq 1.0$	$y=0.018x-3.70$ , R=0.29*	$y=13.2x-3.77$ , R=0.20*
all-sky, $1.0 < z/z_i \leq 2.0$	$y=-0.004x-4.20$ , R=-0.09*	$y=17.6x-4.57$ , R=0.36*
clear-sky, $0.3 \leq z/z_i \leq 2.0$	$y=0.011x-4.04$ , R=0.23*	$y=10.7x-4.13$ , R=0.26*
clear-sky, $0.3 \leq z/z_i \leq 1.0$	$y=0.018x-3.67$ , R=0.30*	$y=11.1x-3.70$ , R=0.17*
clear-sky, $1.0 < z/z_i \leq 2.0$	$y=-0.005x-4.17$ , R=-0.11*	$y=13.8x-4.52$ , R=0.34*
cloudy-sky, $0.3 \leq z/z_i \leq 2.0$	$y=0.009x-4.06$ , R=0.16*	$y=18.5x-4.29$ , R=0.33*
cloudy-sky, $0.3 \leq z/z_i \leq 1.0$	$y=0.018x-3.71$ , R=0.26*	$y=15.5x-3.84$ , R=0.23*
cloudy-sky, $1.0 < z/z_i \leq 2.0$	$y=-0.004x-4.22$ , R=-0.08*	$y=26.2x-4.67$ , R=0.42*

- Deleted: site
- Deleted: <
- Formatted: Space After: 0 pt, Line spacing: single
- Deleted: 0.2
- Deleted: <
- Deleted: 010x
- Deleted: 5
- Deleted: 0.2
- Deleted: <
- Deleted: <
- Deleted: 8
- Deleted: 70
- Deleted: 5
- Deleted: 20
- Deleted: 0.2
- Deleted: <
- Deleted: <
- Deleted: 0
- Deleted: 3
- Deleted: 0.2
- Deleted: <
- Deleted: <
- Deleted: 7
- Deleted: 006x
- Deleted: 6
- Deleted: 2
- Deleted: 0.2
- Deleted: <
- Deleted: <
- Deleted: 009x
- Deleted: 6
- Deleted: 7
- Deleted: 0.2
- Deleted: <
- Deleted: <
- Deleted: 018x
- Deleted: 72
- Deleted: <
- Deleted: 3

1584 **Figures**



1585

1586 **Figure 1.** Spatial distribution of radar wind profiler (RWP) network comprised of six

1587 stations (in black solid circles) on the Tibetan Plateau (TP). The inset map surrounding the

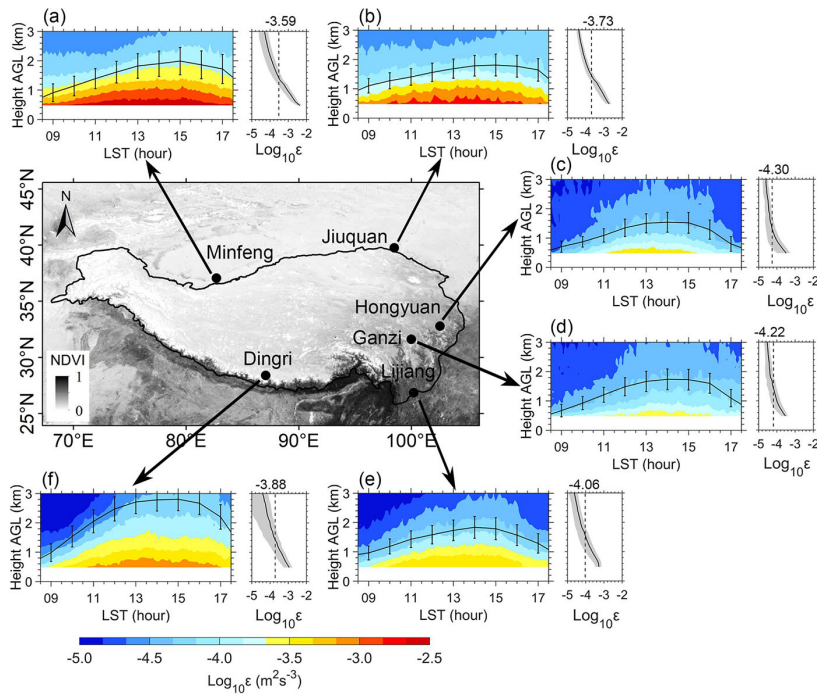
1588 main frame denotes the RGB satellite image from Google Earth that is centered at each

1589 RWP station.

1590

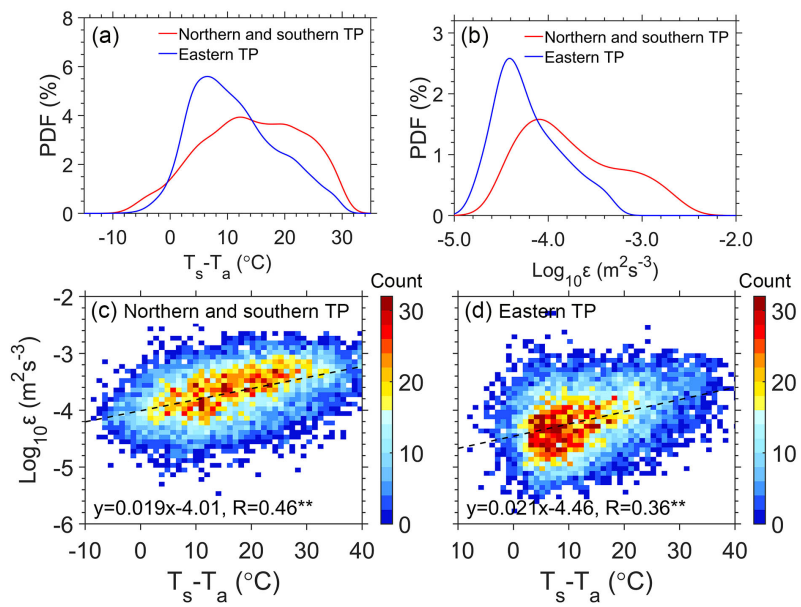
Deleted: site

Deleted: site



1593  
 1594 **Figure 2.** Spatial distribution of the diurnal evolution of the vertical profile of logarithmic  
 1595 turbulence dissipation rate ( $Log_{10}\epsilon$  in color shading, unit:  $m^2 s^{-3}$ ) at 120 m vertical  
 1596 resolution and 6 min intervals, and hourly mean planetary boundary layer height ( $z_i$ , black  
 1597 line, unit: km) during daytime under all-sky conditions from 0900 to 1700 LST for the  
 1598 period September 2022 to October 2023 as retrieved from the profiling measurements at  
 1599 six RWP ~~stations~~ over the TP. The vertical bars indicate the 0.5 standard deviations for  $z_i$ .  
 1600 Also shown on the right-hand side panel are temporally averaged vertical profile of  $\epsilon$  (black  
 1601 line) and its corresponding one standard deviation (gray shading).  
 1602

Deleted: site

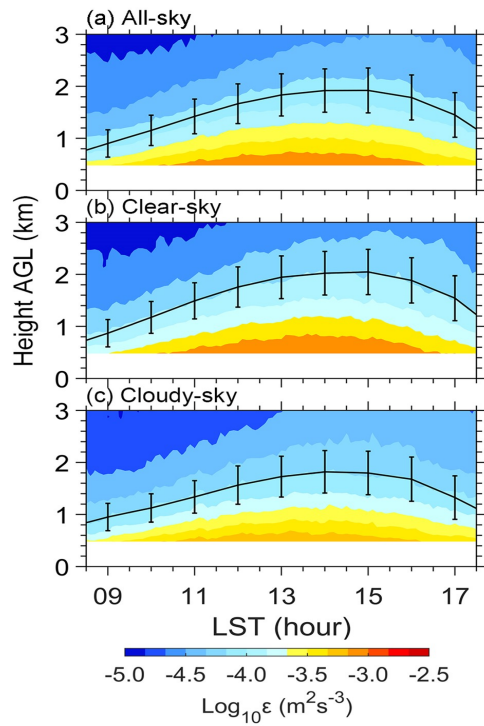


Formatted: Font: (Default) Times New Roman

- Deleted: below
- Deleted: km
- Deleted: and above
- Deleted: 5

1604  
1605  
1606  
1607  
1608  
1609  
1610  
1611  
1612  
1613  
1614  
1615

**Figure 3.** (a) PDF of surface-air temperature difference ( $T_s - T_a$ ) for the northern and southern TP (red line) and eastern TP (blue line), (b) same as (a), but for PDF of  $\text{Log}_{10}\epsilon$  estimated from the measurements of radar wind profilers (RWPs) at the heights ranging from 0.5 to 3.0 km, (c) scatter plots of  $\text{Log}_{10}\epsilon$  as a function of  $T_s - T_a$  in the northern and southern TP, (d) same as (c), but for the eastern TP during daytime under all-sky conditions from 0900 to 1700 local standard time (LST) for the period September 2022 to October 2023. The superscript \*\* for R indicates that the regression slope is statistically significant at  $p < 0.01$  level.

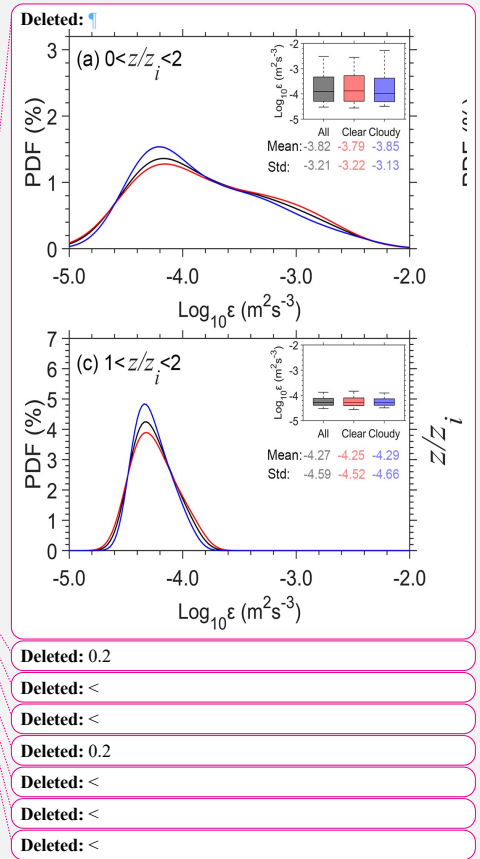
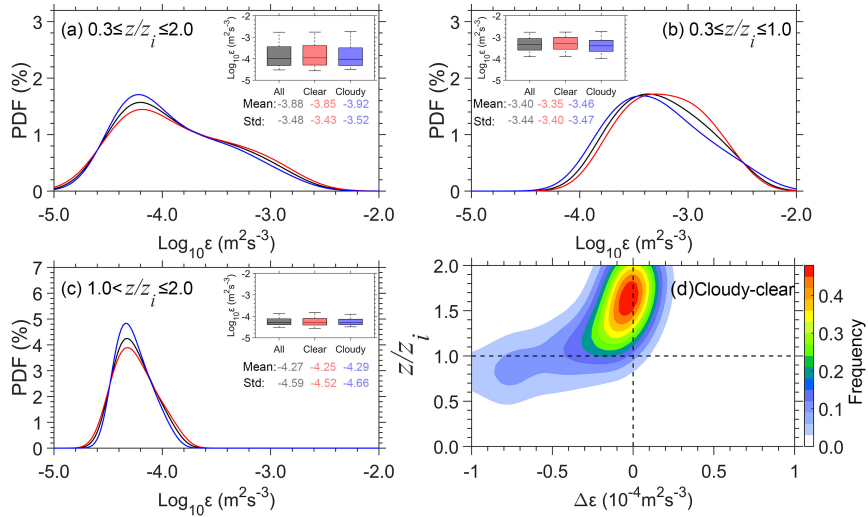


1620

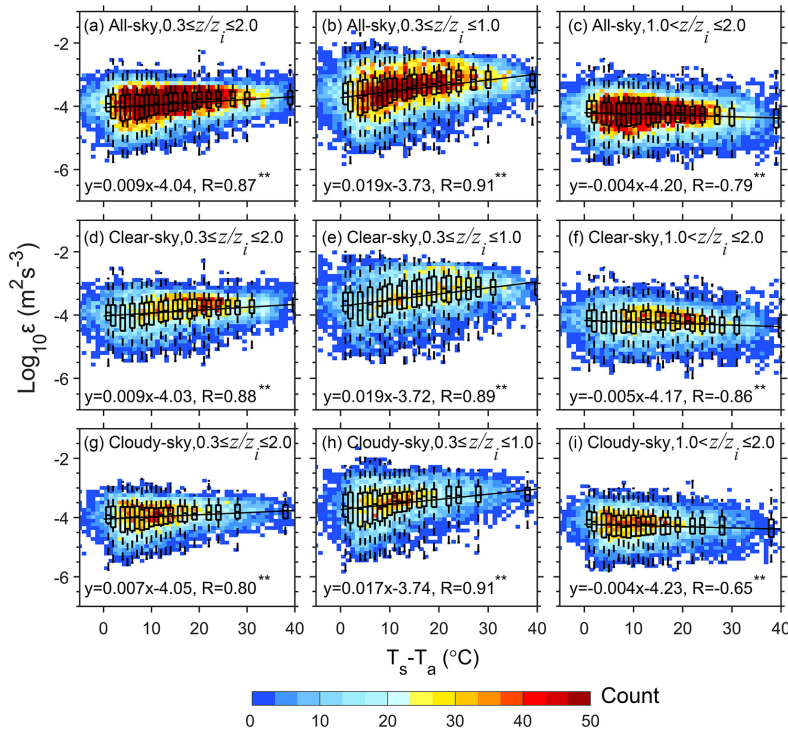
1621 **Figure 4.** Diurnal evolution of the vertical profile of  $\text{Log}_{10} \varepsilon$  (color shading, unit:  $\text{m}^2 \text{s}^{-3}$ )  
 1622 and  $z_i$  (solid line, unit: km) averaged over the six RWP stations over the TP during  
 1623 daytime from 0900 to 1700 LST for the period September 2022 to October 2023 for (a) all-  
 1624 sky conditions, (b) clear-sky conditions and (c) cloudy-sky conditions. The vertical bars  
 1625 indicate the 0.5 standard deviations.

Deleted: site



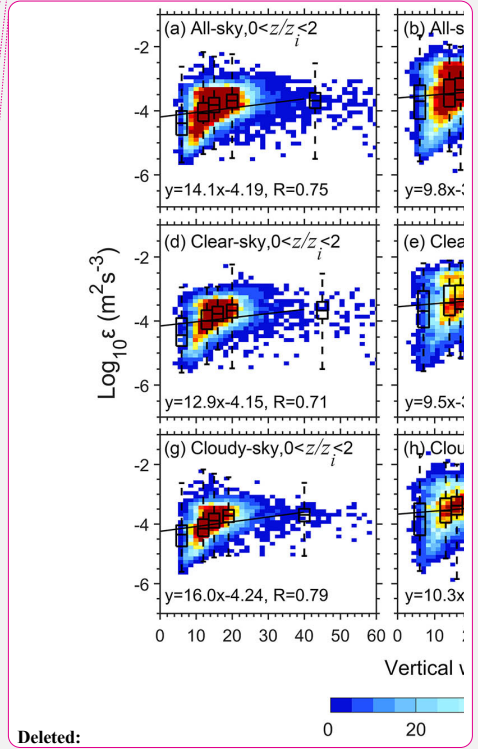


1627  
 1628 **Figure 5.** PDF of daytime  $\text{Log}_{10} \epsilon$  (a) in the whole lower troposphere ( $0.3 \leq z/z_i \leq 2.0$ ), (b)  
 1629 in the PBL ( $0.3 \leq z/z_i \leq 1.0$ ) and (c) above the PBL ( $1.0 < z/z_i \leq 2.0$ ) over the TP under all-  
 1630 sky (black), clear-sky (red) and cloudy-sky (blue) conditions, respectively. (d) Normalized  
 1631 contoured frequency by altitude diagram (NCFAD) for the difference of  $\epsilon$  between cloudy-  
 1632 sky and clear-sky conditions ( $\Delta \epsilon$ ) over the TP. Note that  $z_i$  denotes the depth of the PBL,  
 1633 the height ( $z$ ) and turbulence dissipation rate ( $\epsilon$ ) is normalized by  $z_i$  in order to give a  
 1634 nondimensional vertical coordinate in the form of  $z/z_i$ .  
 1635



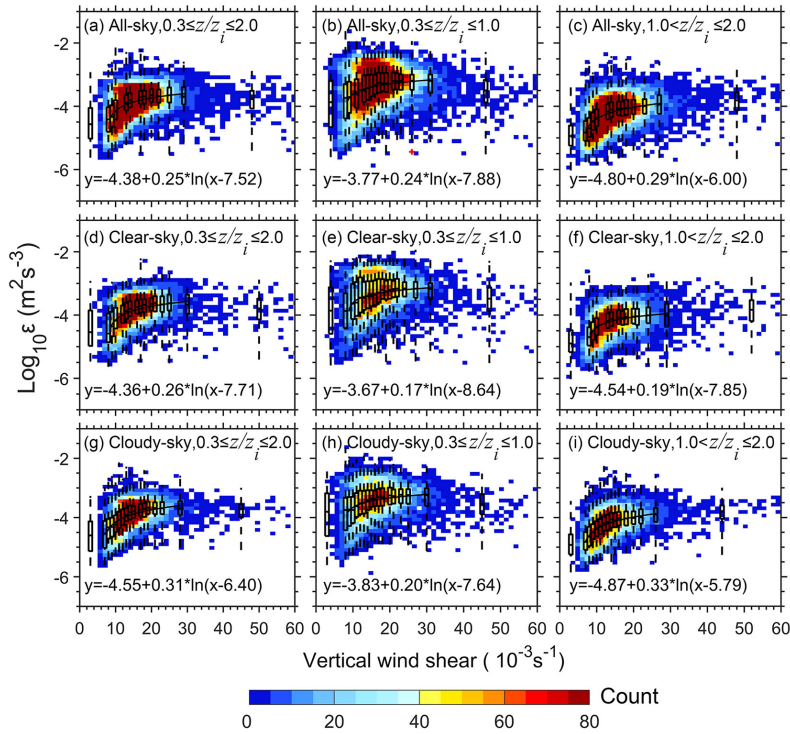
Deleted: ¶ [54]  
Formatted: Font: (Asian) +Body Asian (DengXian)

Deleted: 0.2  
Deleted: <  
Deleted: <  
Deleted: 0.2  
Deleted: <  
Deleted: <  
Deleted: five



Deleted: 0 20

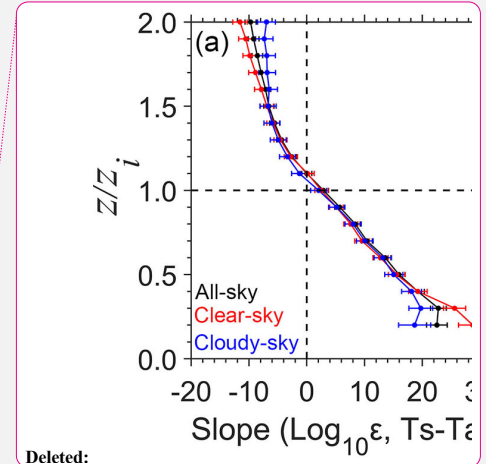
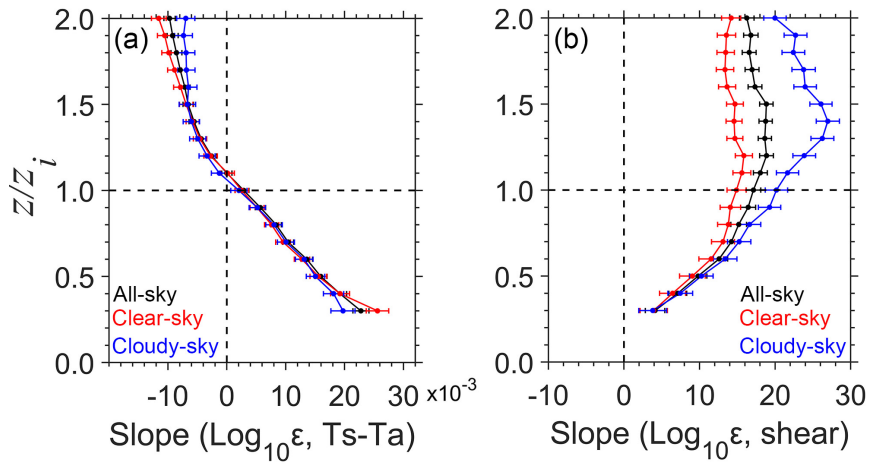
1645  
1646 **Figure 6.** Scatter plots (blue dots) of  $\text{Log}_{10} \varepsilon$  estimated from the measurements of RWPs  
1647 in the whole lower troposphere ( $0.3 \leq z/z_i \leq 2.0$ , a, d, g), in the PBL ( $0.3 \leq z/z_i \leq 1.0$ , b, e, h)  
1648 and above the PBL ( $1.0 < z/z_i \leq 2.0$ , c, f, i) over the TP as a function of  $T_s - T_a$  under all-  
1649 sky (a-c), clear-sky (d-f) and cloudy-sky conditions (g-i), respectively. Also overlaid are  
1650 their corresponding box and whisker plots and regression linear equations and correlation  
1651 coefficients in each panel, where all  $T_s - T_a$  samples are divided into twenty bins, each of  
1652 which has the same sample size. Note that the median is shown as a line whereas the outer  
1653 boundaries of the boxes represent 25 and 75 quartiles and the dashed lines present  
1654 interquartile range (IQR). The superscripts \* and \*\* for R indicate that the regression slopes  
1655 are statistically significant at  $p < 0.05$  and  $p < 0.01$  levels, respectively.  
1656



1669  
1670  
1671  
1672  
1673  
1674  
1675  
1676  
1677  
1678

**Figure 7.** Scatter plots of  $\text{Log}_{10} \varepsilon$  estimated from the measurements of RWPs in the whole lower troposphere ( $0.3 \leq z/z_i \leq 2.0$ , a, d, g), in the PBL ( $0.3 \leq z/z_i \leq 1.0$ , b, e, h) and above the PBL ( $1.0 < z/z_i \leq 2.0$ , c, f, i) over the TP as a function of vertical wind shear (VWS) under all-sky (a-c), clear-sky (d-f) and cloudy-sky conditions (g-i), respectively. Also overlaid are their corresponding box and whisker plots and fitting equations in each panel, where all VWS samples are divided into twenty bins, each of which has the same sample size. Note that the median is shown as a line whereas the outer boundaries of the boxes represent 25 and 75 quartiles and the dashed lines present interquartile range (IQR).

- Formatted: Font: Not Bold, Not Italic
- Formatted: Font: Not Bold
- Formatted: Font: Not Bold, Not Italic
- Formatted: Font: Not Bold, Not Italic
- Formatted: Font: Not Bold, Not Italic
- Formatted: Font: Not Bold, Not Italic
- Formatted: Font: Not Bold
- Formatted: Font: Not Bold, Not Italic
- Deleted: Same as Figure 5, but for  $\text{Log}_{10} \varepsilon$  as a function of vertical wind shear (VWS)

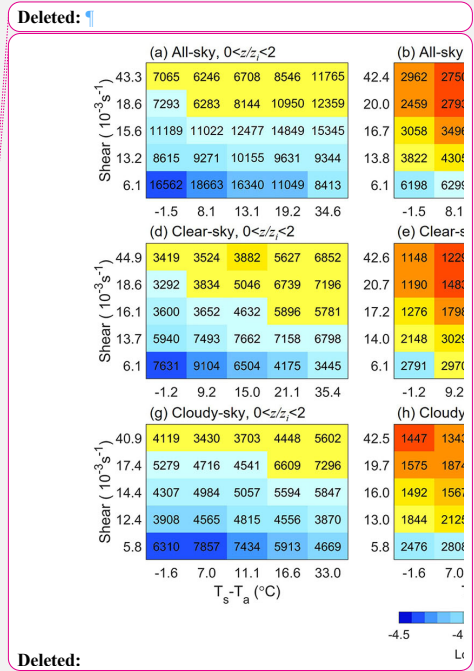
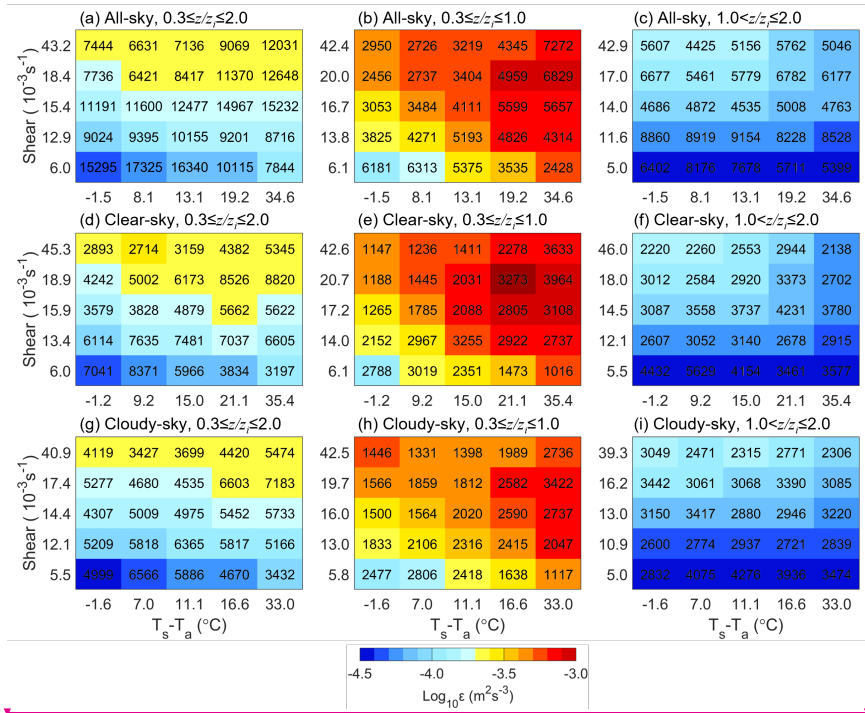


Deleted:

Formatted: Justified

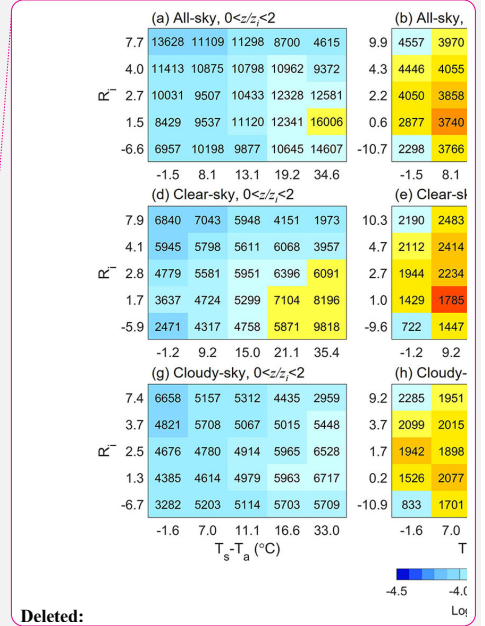
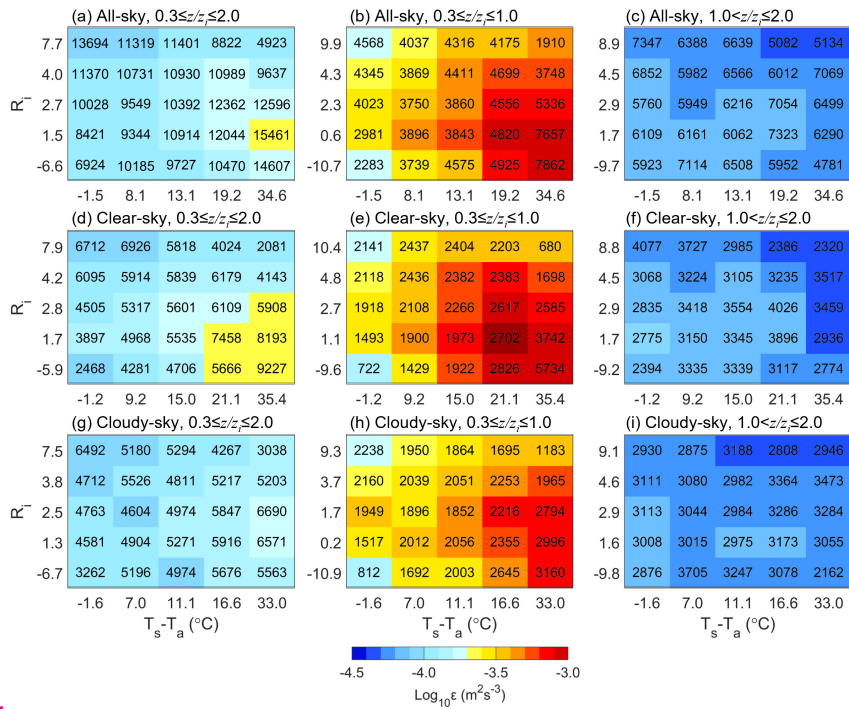
Deleted: vertical wind shear

1681  
 1682 **Figure 8.** The vertical profiles of least squares regression slope between  $\text{Log}_{10}\epsilon$  and  
 1683  $T_s - T_a$  (a) and **VWS** (b) over the TP under all-sky (black), clear-sky (red) and cloudy-sky  
 1684 (blue) conditions, respectively.



Deleted: vertical wind shear

1687  
 1688 **Figure 9.** Joint dependence of  $\text{Log}_{10}\epsilon$  (color shading) on the  $\text{VWS}$  and  $T_s - T_a$  within  
 1689 and above the PBL (a, d, g), in the PBL (b, e, h) and above the PBL (c, f, i) over the TP  
 1690 under all-sky (a-c), clear-sky (d-f) and cloudy-sky (g-i) conditions, respectively. The  
 1691 number given in each panel is the total number of samples used.



Deleted:

1695

1696 **Figure 10.** Joint dependence of  $\text{Log}_{10}\epsilon$  (color shading) on the gradient Richardson  
 1697 number ( $Ri$ ) and  $T_s - T_a$  in and above the PBL (a, d, g), in the PBL (b, e, h) and above  
 1698 the PBL (c, f, i) over the TP under all-sky (a-c), clear-sky (d-f) and cloudy-sky (g-i)  
 1699 conditions, respectively. The number given in each panel is the total number of samples  
 1700 used.

Page 8: [1] Formatted mengdeli 07/06/2024 10:05:00

Font: Not Italic

Page 8: [2] Formatted mengdeli 07/06/2024 10:05:00

Font: Not Italic

Page 8: [3] Formatted mengdeli 07/06/2024 10:05:00

Font: Not Italic

Page 8: [4] Deleted JG 07/06/2024 17:06:00

Page 8: [4] Deleted JG 07/06/2024 17:06:00

Page 8: [4] Deleted JG 07/06/2024 17:06:00

Page 8: [5] Formatted mengdeli 07/06/2024 10:05:00

Font: Not Italic

Page 8: [6] Formatted mengdeli 07/06/2024 10:05:00

Font: Not Italic

Page 8: [7] Formatted mengdeli 07/06/2024 10:05:00

Font: Not Italic

Page 8: [8] Deleted JG 07/06/2024 17:12:00

Page 8: [9] Formatted mengdeli 07/06/2024 10:05:00

Font: Not Italic

Page 8: [9] Formatted mengdeli 07/06/2024 10:05:00

Font: Not Italic

Page 8: [10] Deleted JG 07/06/2024 17:02:00

Page 8: [10] Deleted JG 07/06/2024 17:02:00

Page 8: [11] Formatted mengdeli 07/06/2024 10:05:00

Font: Not Italic

Page 8: [12] Deleted JG 07/06/2024 17:03:00

Page 8: [12] Deleted JG 07/06/2024 17:03:00



▲  
Page 8: [12] Deleted JG 07/06/2024 17:03:00  
▼

▲  
Page 8: [13] Formatted mengdeli 07/06/2024 10:05:00  
Font: Not Italic

▲  
Page 8: [14] Deleted JG 09/06/2024 10:34:00  
▼

▲  
Page 8: [14] Deleted JG 09/06/2024 10:34:00  
▼

▲  
Page 8: [15] Deleted deli meng 07/06/2024 01:18:00  
▼

▲  
Page 8: [15] Deleted deli meng 07/06/2024 01:18:00  
▼

▲  
Page 8: [16] Deleted JG 07/06/2024 17:20:00  
▼

▲  
Page 8: [16] Deleted JG 07/06/2024 17:20:00  
▼

▲  
Page 8: [16] Deleted JG 07/06/2024 17:20:00  
▼

▲  
Page 8: [17] Deleted JG 09/06/2024 10:34:00  
▼

▲  
Page 8: [17] Deleted JG 09/06/2024 10:34:00  
▼

▲  
Page 8: [18] Deleted JG 07/06/2024 17:24:00  
▼

▲  
Page 8: [18] Deleted JG 07/06/2024 17:24:00  
▼

▲  
Page 8: [18] Deleted JG 07/06/2024 17:24:00  
▼

▲  
Page 8: [18] Deleted JG 07/06/2024 17:24:00  
▼



Page 8: [19] Deleted JG 07/06/2024 17:27:00

Page 8: [20] Formatted mengdeli 07/06/2024 10:05:00

Font: Not Italic

Page 8: [20] Formatted mengdeli 07/06/2024 10:05:00

Font: Not Italic

Page 8: [21] Formatted mengdeli 07/06/2024 10:05:00

Font: Not Italic

Page 8: [22] Formatted mengdeli 07/06/2024 10:05:00

Font: Not Italic

Page 8: [23] Deleted JG 07/06/2024 17:32:00

Page 8: [24] Formatted mengdeli 07/06/2024 10:05:00

Font: Not Italic

Page 8: [25] Formatted mengdeli 07/06/2024 10:05:00

Font: Not Italic

Page 8: [26] Formatted mengdeli 07/06/2024 10:05:00

Font: Not Italic

Page 8: [26] Formatted mengdeli 07/06/2024 10:05:00

Font: Not Italic

Page 8: [27] Formatted mengdeli 07/06/2024 10:05:00

Font: Not Italic

Page 8: [28] Deleted JG 07/06/2024 17:27:00

Page 8: [28] Deleted JG 07/06/2024 17:27:00

Page 8: [29] Deleted JG 07/06/2024 17:27:00

Page 8: [29] Deleted JG 07/06/2024 17:27:00

Page 8: [30] Deleted JG 07/06/2024 17:29:00

Page 8: [30] Deleted JG 07/06/2024 17:29:00

▲ Page 8: [30] Deleted JG 07/06/2024 17:29:00

▲ Page 8: [31] Formatted mengdeli 07/06/2024 10:05:00

Font: Not Italic

▲ Page 13: [32] Deleted mengdeli 06/05/2024 11:31:00

▲ Page 13: [32] Deleted mengdeli 06/05/2024 11:31:00

▲ Page 13: [33] Deleted mengdeli 05/06/2024 16:28:00

▲ Page 13: [33] Deleted mengdeli 05/06/2024 16:28:00

▲ Page 13: [34] Deleted JG 04/06/2024 18:44:00

▲ Page 13: [35] Formatted JG 09/06/2024 11:35:00

Font: (Asian) Times New Roman, Not Highlight

▲ Page 13: [35] Formatted JG 09/06/2024 11:35:00

Font: (Asian) Times New Roman, Not Highlight

▲ Page 13: [35] Formatted JG 09/06/2024 11:35:00

Font: (Asian) Times New Roman, Not Highlight

▲ Page 13: [36] Formatted mengdeli 07/06/2024 10:05:00

Not Highlight

▲ Page 13: [36] Formatted mengdeli 07/06/2024 10:05:00

Not Highlight

▲ Page 13: [37] Deleted JG 09/06/2024 11:07:00

▲ Page 13: [37] Deleted JG 09/06/2024 11:07:00

▲ Page 13: [38] Deleted JG 09/06/2024 11:46:00

▲ Page 13: [38] Deleted JG 09/06/2024 11:46:00

▲ Page 13: [38] Deleted JG 09/06/2024 11:46:00

▲ Page 13: [39] Formatted mengdeli 07/06/2024 10:05:00

Not Highlight

Page 13: [39] Formatted mengdeli 07/06/2024 10:05:00

Not Highlight

Page 13: [40] Deleted JG 09/06/2024 11:47:00

Page 13: [40] Deleted JG 09/06/2024 11:47:00

Page 13: [41] Formatted mengdeli 07/06/2024 10:05:00

Not Highlight

Page 13: [41] Formatted mengdeli 07/06/2024 10:05:00

Not Highlight

Page 13: [42] Deleted JG 09/06/2024 11:46:00

Page 13: [42] Deleted JG 09/06/2024 11:46:00

Page 13: [43] Deleted mengdeli 05/06/2024 16:58:00

Page 13: [44] Deleted mengdeli 05/06/2024 17:02:00

Page 13: [44] Deleted mengdeli 05/06/2024 17:02:00

Page 13: [45] Deleted mengdeli 05/06/2024 17:05:00

Page 13: [46] Deleted mengdeli 05/06/2024 17:02:00

Page 13: [46] Deleted mengdeli 05/06/2024 17:02:00

Page 17: [47] Deleted mengdeli 06/05/2024 11:33:00

Page 17: [47] Deleted mengdeli 06/05/2024 11:33:00

▲  
▼  
**Page 17: [47] Deleted      mengdeli      06/05/2024 11:33:00**

▲  
▼  
**Page 17: [47] Deleted      mengdeli      06/05/2024 11:33:00**

▲  
▼  
**Page 17: [47] Deleted      mengdeli      06/05/2024 11:33:00**

▲  
▼  
**Page 17: [47] Deleted      mengdeli      06/05/2024 11:33:00**

▲  
▼  
**Page 17: [48] Deleted      mengdeli      07/06/2024 10:03:00**

▲  
▼  
**Page 17: [48] Deleted      mengdeli      07/06/2024 10:03:00**

▲  
▼  
**Page 17: [49] Deleted      mengdeli      02/06/2024 23:24:00**

▲  
▼  
**Page 17: [49] Deleted      mengdeli      02/06/2024 23:24:00**

▲  
▼  
**Page 17: [50] Deleted      mengdeli      05/06/2024 17:02:00**

▲  
▼  
**Page 17: [50] Deleted      mengdeli      05/06/2024 17:02:00**

▲  
▼  
**Page 17: [51] Deleted      mengdeli      07/06/2024 10:03:00**

▲  
▼  
**Page 17: [51] Deleted      mengdeli      07/06/2024 10:03:00**

▲  
▼  
**Page 17: [51] Deleted      mengdeli      07/06/2024 10:03:00**

▲  
▼  
**Page 17: [52] Deleted      mengdeli      07/06/2024 10:03:00**

▲ Page 17: [52] Deleted    mengdeli    07/06/2024 10:03:00

▼  
▲ Page 17: [52] Deleted    mengdeli    07/06/2024 10:03:00

▼  
▲ Page 17: [52] Deleted    mengdeli    07/06/2024 10:03:00

▼  
▲ Page 17: [52] Deleted    mengdeli    07/06/2024 10:03:00

▼  
▲ Page 17: [52] Deleted    mengdeli    07/06/2024 10:03:00

▼  
▲ Page 17: [53] Deleted    mengdeli    05/06/2024 17:02:00

▼  
▲ Page 17: [53] Deleted    mengdeli    05/06/2024 17:02:00

▼  
▲ Page 38: [54] Deleted    mengdeli    05/06/2024 22:20:00

▼  
▲